Josef Franz Viktor Tausendschön, BSc

Sedimentation Behavior of Wet Particulate Systems

Masterarbeit

zur Erlangung des akademischen Grades

Diplom-Ingenieur

eingereicht an der

Technischen Universität Graz

Betreuer:

Ass.Prof. Priv.-Doz. Dipl.-Ing. Dr.techn. Stefan Radl

Institut für Prozess- und Partikeltechnik

Graz, Mai 2018

EIDESSTATTLICHE ERKLÄRUNG

Ich erkläre an Eides statt, dass ich die vorliegende Arbeit selbstständig verfasst, andere als die angegebenen Quellen/Hilfsmittel nicht benutzt, und die den benutzten Quellen wörtlich und inhaltlich entnommenen Stellen als solche kenntlich gemacht habe. Das in TUGRAZonline hochgeladene Textdokument ist mit der vorliegenden Masterarbeit identisch.

Datum	Unterschrift

Acknowledgement

I would like to express my sincere gratitude to Ass. Prof. Priv.-Doz. Dr. Stefan Radl, who supervised this work with dedication, guided my scientific development and highly engaged himself to enable my research stay at the Princeton University.
A special thanks to Prof. Dr. Sankaran Sundaresan and Dr. Jari Kohlemainen for collaboration and mentoring throughout my stay at the Princeton University.
I would like to acknowledge and thank the Graz University of Technology for financial support and for allowing me to conduct my research.

First and foremost, I am thankful in the highest possible way to my mother, Marianne Tausendschön, for her staggering passion, for her commitment, for the successful attempt to keep all negativity off and for pushing the boundaries, while still providing all vital things.
I am overwhelmed with thankfulness to my sister Dr. Isabel Tausendschön for being a role model, for supporting me in all possible ways, for showing more passion on my work and interests than on her own, and especially for always excellent scientific advice.
Also I would like to thank my father, Josef Tausendschön who always wanted the best for me, for his support.

Abstract

Euler-Lagrange (EL) based simulations of industrial scaled processes demand very high computational resources, especially for wet gas-particle systems. As a consequence, some sort of coarse-graining (CG) to reduce the number of tracked particles is necessary. Two different scaling laws, taking liquid bridges and cohesive forces into account, were investigated for the usage in EL-based simulations. The coarse-graining models based on (i) constant stresses and (ii) invariant key numbers were compared to (iii) a coarse-graining model without scaling of the cohesive forces.

The outcome of the different scaling strategies was verified against data from the original systems (without CG) considering (i) a wet fluidized bed, and (ii) the sedimentation of wet particles in a fully periodic domain. The results indicate that the maximum pressure drop of a fluidized bed is not improved by a scaling of the cohesive forces. In the cohesive dominated regime, the closest approximation of the original bed height is obtained when using the scaling based on a constant Bond number. The results for the domain average slip velocity in the periodic domain confirmed that the Bond number-based scaling achieves the smallest deviations to the original system. Although, this is only valid for small coarse-graining ratios, at higher ratios the nonlinear adaption of the cohesive parameters led to a significant overprediction of the cohesive force and therefore big particle clusters.

Kurzfassung

Simulationen von Prozessen im Industriemaßstab auf Basis von Euler-Lagrange (EL) Betrachtungen erfordern einen sehr großen Rechenaufwand, insbesondere für feuchte Gas-Partikel-Systeme. Um solche Simulationen durchführen zu können ist es notwendig die Anzahl an betrachteten Partikeln zu reduzieren. Für den Einsatz in EL-basierten Simulationen - unter der Berücksichtigung von Flüssigbrücken und kohäsiven Kräften - wurden zwei verschiede Skalierungen untersucht. Diese Skalierungsmodelle basierend auf konstanten Spannungen bzw. konstanten Bond-zahlen, werden mit einem vergrößerten System ohne Skalierung der kohäsiven Kräfte verglichen. Die Ergebnisse der verschiedenen Skalierungsstrategien aus (i) den Simulationen einer feuchten Wirbelschicht, sowie (ii) der Sedimentation in einer vollkommen periodischen Box wird mit (iii) dem jeweiligen Basissystem (ohne Skalierung) verifiziert.

Hinsichtlich des maximalen Druckverlustes einer Wirbelschicht wurde kein Hinweis gefunden, dass die Skalierung der kohäsiven Kräfte automatisch in einer besseren Wiedergabe des Basissystems resultiert. In kohäsiv dominierten Regimen bildet die Bond-Zahl-basierte Vergrößerung die Betthöhe der Wirbelschicht am genauesten nach. Die Ergebnisse der Schlupfgeschwindigkeit der periodischen Simulationen bestätigen die Erkenntnis, dass die Bond-Zahl-basierte Skalierung die beste Reproduktion des Originalsystems liefert. Dies ist jedoch nur gültig für kleine Skalierungsraten, da die nichtlineare Skalierung der Kohäsions-Parameter in die Bildung großer Partikel-Cluster resultiert.

Table of Content

1. Introduction

Wet particulate systems, such as agitated wet granular matter or fluidized wet particles, play an important role in a variety of industrial processes. Examples are chemical processes like cracking of hydrocarbons [1], or at the usage of wet powders in the pharmaceutical industry [2]. For this reason, the investigation of the flow characteristics in these industrial processes is essential for the equipment design, or the optimal operation of a process.

This section provides an overview of the challenges and the background that are associated with the modeling and simulation of wet particulate systems. It further describes the state of the art in this field and explains the goal of the present study.

1.1. Challenges and background

The occurrence of coherent, inhomogeneous flow structures (often called "mesoscale structures") affects essential process characteristics already in dry systems at a fundamental level [3,4]. Even more challenging are wet systems: the addition of liquid, or the use of wet particles, increases the complexity of the system behavior. The presence of a liquid film on the particles enables liquid bridge formation during particle–particle or particle–wall interactions. These liquid bridges may cause wanted or unwanted agglomeration [5].

The flow structure is impeded by agglomerates, which leads to slumping or roughening of the fluidization process. Overall, these phenomena affect key characteristics like the heat or mass transfer and can influence chemical reactions. This impact on fluidization has been explored by several researchers [6,7,8,9,10].

Mesoscale structures emerge over a wide span of time and length scales [4]. As a consequence, it is computationally expensive to resolve these structures fully. To investigate these characteristics of wet particle flow in the presence of gas, three appropriate methods are basically available: (i) Direct Numerical Simulation (DNS), (ii) Euler–Euler (EE), and (iii) Euler–Lagrange (EL) methods [11].

In DNS, all particles are individually observed and the fluid around the particles is completely resolved. Newton's equation of motion is solved for each particle and the Navier–Stokes equation in its most fundamental form is solved for the interstitial fluid [12]. Because of this complex and computational demanding approach, DNS is

limited to small systems (typically a few thousand particles, up to at most 1 Million particles). DNS is mainly used for the simulation of microscale flow features to derive closures for other simulation approaches.

The EE method, commonly referred to as the two-fluid model (TFM), treats both phases as continua. TFMs rely on solving locally averaged equations [13,14]. This concept fits well for large-scale flow characteristics, although constitutive models are needed for the force between the two phases, and for the effective stress in each phase. TFMs are adequate for dry systems [13,15]. However, a complete set of constitutive models is not available for wet systems yet [11].

In some sense, the EL approach combines DNS and EE by solving locally averaged equations for the fluid phase and tracking individual particles via Newton's equation of motion [16][17]. Thus, the EL approach also requires constitutive models for the fluid–particle interaction force.

Deen et al. [15] investigated the hard- and soft-sphere approach for the modeling of particle–particle interactions, which are applicable for EL and DNS. Commonly used for the soft-sphere approach is the Discrete Element Method (DEM) of Cundall and Strack [18], which is applied in the present work as well.

To study mesoscale structures in wet systems looking at particles as discrete objects, as done in the EL simulations, is an attractive approach. The reason, therefore, lay in the fact that the implementation of the formation and rupture of liquid bridges in this modeling approach is straightforward [11]. Models, which describe interaction forces between colliding particles, have been presented by Mikami et al. [19] for the capillary force and by Pitois et al. [20] for viscous effects. The rupture of the liquid bridge was described by Lian et al. [21] and the redistribution of the unbound liquid was in the focus of several studies [22,23,24]. Taking into account the described advantages, the EL method is used in this study. In the literature, this approach is commonly known as the Computational Fluid Dynamics–Discrete Element Method (CFD–DEM) [25].

Nowadays, EL simulations with several million particles can be performed with standard computer clusters. To observe industrial scale processes with up to a few billion particles some kind of coarse-graining, which reduces the number of particles to be tracked, is necessary. Such a coarse-graining approach requires deeper

thoughts on how particle-fluid and particle-particle interaction models should be implemented. Specifically, there are two different strategies of reducing the number of tracked particles in EL-based simulations: (i) using so-called "parcels" that consist of a certain number of small particles and are modeled as solid spheres [26], or (ii) by applying the Multiphase Particle-In-Cell method (MPI-PIC) [27]. The former is often referred to as the Discrete Parcel Method (DPM), which is reviewed in greater detail in Section 1.2 below. DPM only tracks a fraction of the particles, but accounts for parcel-parcel collision using classical (DEM-inspired) contact force models. In contrast, MPI-PIC neither tracks all particles, nor their collisions. Instead a (discrete) approximation of the particle distribution is performed via test particles.

Another option to reduce the computational cost associated with simulations is the coarsening of the fluid phase [28]. However, the cost assigned to the solution of fluid phase transport equations are typically much lower than the cost of solving the particle phase. Thus, for the present study fluid coarsening has not been addressed in greater detail.

1.2. Background on the Discrete Parcel Method

A parcel approach for the simulation of dry gas–particle flows was presented by Radl et al. [26]. In addition, the influence of the discrete parcel method (DPM) on the drag force was investigated in a previous study [29]. The use of the coarse-grained soft-sphere approach in industrial applications was reviewed recently by Radl and Municchi [30].

Bierwisch et al. [31] presented a coarse-graining approach for the dynamics of powders in cavity filling. For dilute systems, the coarse-graining scheme was based on force scaling, and for dense systems it was based on stress scaling. In general, the idea was to preserve the energy density and the evolution of the energy density of the original system. It was shown that the scaling must be based on the following scaling-invariant factors: particle density, friction coefficients, Young's modulus, and coefficient of restitution. Cohesion effects were represented in a simplified way by considering a JKR model.

A large-scale DEM of a 2D fluidized bed was performed by Sakai et al. [32], in which particle–wall interactions were not taken into account. The so-called "direct force scaling" method was used with quadratic scaling of the cohesive force and cubic

scaling of the contact forces. In this simplified set-up - cohesive interactions were expressed with van der Waals forces - the coarse-grained system imitated the original case precisely.

Chan et al. [33] applied a similar coarse-graining model to wet particle flow in a mixer. The liquid bridge force was scaled quadratic in this study and was considered only between particles, while the effects on particle interactions with walls and the impeller were neglected. The coarse-graining model used was validated for reproducing the original bulk flow and mixing behavior.

Thakur et al. [34] considered the scaling of DEM model parameters for cohesive and noncohesive systems in a uniaxial compression test. They stated that a linear scaling of the particle stiffness and a quadratic scaling of the adhesive force can reproduce the bulk properties of the basic system with the primary particles sufficiently.

A subtle, but eventually important detail related to EL-based simulations is the rolling friction. Goniva et al. [35] showed the influence of the rolling friction model on CFD–DEM simulations of a fluidized bed. Therefore, different rolling friction models were tested, with the key conclusion that a simple rolling friction model should be used for such applications.

1.3. Goals

The focus of the present thesis is on presenting a coarse-graining approach for wet particulate systems that allows precise DPM-based simulation of these systems. A specific focus is on particle–wall interactions, since these have not been detailed in greater depth in literature. Also the coarse-graining approach should be suitable for the following three flow situations: (i) the filling and the emptying of a box with wet (cohesive) powder, (ii) the fluidization of wet granular material, and (iii) the sedimentation of wet particles. The verification of the coarse-grained model is obtained by comparing the results of the DPM-based simulations with data from the original particle system, i.e., a DEM-based simulation.

1.4. Thesis structure

The simulation method, as well as closures for contact and liquid bridge forces, are described in Chapter 2. The coarse-graining approach, considering different scaling strategies, is explained in Chapter 3. The preliminary results, which describe the outcome of the rolling friction tests and of the simulations made for testing the coarse graining of the solid phase, are provided in Chapter 4. Chapter 5 discusses the main results and findings of the present study. Chapter 6 provides a conclusion.

2. Simulation Method

As described in the previous chapter, the CFD–DEM approach is used in this work. The CFD part is realized within the framework of OpenFOAM® [36] and the DEM part is solved using LIGGGHTS® [37]. The coupling between these two solvers is performed with CFDEM® [37].

The translational and rotational motion of the particles is described by:

$$m_i \frac{d\boldsymbol{v}_{p,i}}{dt} = \sum_j \left(\boldsymbol{F}^n_{cont,ij} + \boldsymbol{F}^t_{cont,ij} + \boldsymbol{F}_{coh}\right) + m_i\, \boldsymbol{g} + \boldsymbol{F}_{drag,g\to p} \tag{1}$$

$$I_i \frac{d\boldsymbol{\omega}_i}{dt} = \boldsymbol{T}_i \tag{2}$$

m_i is the solid mass of the particle i. Because of the small contribution, the mass of the liquid adhering to the particle surface is neglected. $\boldsymbol{v}_{p,i}$ is the translational velocity of the particle. $\boldsymbol{F}^n_{cont,ij}$ and $\boldsymbol{F}^t_{cont,ij}$ are the normal and tangential contact forces, while $\boldsymbol{F}_{drag,g\to p}$ represents the interaction force between the gas and the particle. $\boldsymbol{F}_{coh}$ is the cohesive force acting on the particles and is defined as the sum of the capillary force $\boldsymbol{F}_{cap}$ and the viscous force $\boldsymbol{F}_{vis}$. The total torque $\boldsymbol{T}_i$ on each particle is equal to the moment of inertia I_i and the change in the angular velocity $\boldsymbol{\omega}_i$. This form used for the rotational degree of freedom is valid for spheres only, which is acceptable for most of the systems under consideration.

2.1. Closures for contact forces

Particles are represented as soft spheres, and their deformations are represented by idealized closure models based on overlaps. Specifically, for the tangential and normal particle interaction, a spring–dashpot-slider model will be used.

2.1.1. Normal force contact model

In a dense system, the normal contact force is described by:

$$\boldsymbol{F}^n_{cont,ij} = k_n\, \delta_n\, \boldsymbol{n}_{ij} + c_n\, \dot{\delta}_n\, \boldsymbol{n}_{ij} \tag{3}$$

In equation 3, k_n is the normal stiffness of the particle, c_n the normal damping coefficient, and δ_n the normal particle overlap. $\boldsymbol{n}_{ij}$ is the unit normal vector between the colliding particles i and j.

2.1.2. Tangential force contact model

The tangential contact force is modeled with:

$$\boldsymbol{F}^{t}_{cont,ij} = \min\left(\left|\boldsymbol{F}^{n}_{cont,ij}\right| \mu_r \, \boldsymbol{t}_{ij} \, , k_t \, \delta_t \, \boldsymbol{t}_{ij} + \, c_t \, \dot{\delta}_t \, \boldsymbol{t}_{ij}\right) \tag{4}$$

μ_r represents the rolling friction coefficient, k_t is the tangential stiffness, c_t is the tangential damping coefficient, and δ_t stands for the tangential overlap. $\boldsymbol{t}_{ij}$ is the unit tangential normal vector.

2.1.3. Rolling friction model

Different rolling friction models were tested in the pure granular flow tests. Ai et al. [38] made an assessment of different rolling friction models used in DEM simulations and classified them into four characteristic categories. Also contact independent models (Model D) were reviewed, but rejected at the outset, because of the contact pair torques that are not in equilibrium.

a) Model A: directional constant torque

Bierwisch et al. [31] used a Coulomb-like rolling friction model, which corresponds to the model A in [38]. They also noted that long-term relaxations can occur when using this dynamic rolling friction model but did not consider any stabilizing strategies in their work [31]. In the directional constant torque models, the torque acting between two particles $\boldsymbol{M}_r$ is expressed as:

$$\boldsymbol{M}_r = -\frac{\boldsymbol{\omega}_{rel}}{|\boldsymbol{\omega}_{rel}|} \, \mu_r \, R_{eff} \, \boldsymbol{F}_n \tag{5}$$

$$\boldsymbol{\omega}_{rel} = \boldsymbol{\omega}_i - \boldsymbol{\omega}_j \, , R_{eff} = \frac{R_i \, R_j}{(R_i + R_j)} \tag{6),(7}$$

R_{eff} is the effective particle radius and $\boldsymbol{\omega}_{rel}$ the relative angular velocity between particle i and particle j.

b) Model B: viscous models (CDT)

A term related to the angular velocity is added to model A to form so-called viscous (-based) torque models. This model is referred to as “CDT” in LIGGGHTS®.

$$\boldsymbol{M}_r = -\mu_r \, R_{eff} \, \boldsymbol{F}_n \left(\boldsymbol{\omega}_i \, R_i - \boldsymbol{\omega}_j \, R_j\right) \tag{8}$$

This description of the rolling friction is often used in literature, e.g., as done by Radl et al. [26], and used in parcel-based approaches for gas–particle flows.

c) Model C.1: elastic-plastic spring–dashpot model (EPSD)

In the elastic-plastic spring–dashpot model the total rolling resistance torque is calculated as:

$$\boldsymbol{M}_r = \boldsymbol{M}_r^d + \boldsymbol{M}_r^k \tag{9}$$

The spring torque $\boldsymbol{M}_r^k$ is determined via an incremental torque using the rolling stiffness k_r and the increment in the relative particle-particle contact angle $\Delta\theta_r$:

$$\Delta M_r^k = -k_r \, \Delta\theta_r \tag{10}$$

$$k_r = 2.25 \, k_n \, R_{eff}^2 \, \mu_r^2 \tag{11}$$

The viscous damping torque M_r^d is also summed up from an incremental torque with (for further information of the EPSD model and the calculation of $\boldsymbol{M}_r^m$ see Appendix A.1):

$$M_{r,t+\Delta t}^d = \begin{cases} -c_r \, \dot{\theta}_r \; if \left| M_{r,t+\Delta t}^k \right| < \boldsymbol{M}_r^m \\ -f \; c_r \, \dot{\theta}_r \; if \left| M_{r,t+\Delta t}^k \right| = \boldsymbol{M}_r^m \end{cases} \tag{12}$$

d) Model C.2: elastic-plastic spring–dashpot model 2 (EPSD2)

In the EPSD2 model, the viscous damping torque $\boldsymbol{M}_r^d$ is neglected. Therefore, the total rolling resistance torque $\boldsymbol{M}_r$ simplifies to:

$$\boldsymbol{M}_r = M_r^k \tag{13}$$

In contrast to the EPSD model, the rolling stiffness is defined by:

$$k_r = k_t \, R_{eff}^2 \tag{14}$$

2.2. Closures accounting for the presence of liquid bridges

The formation or rupture of liquid bridges is dependent on the distance between the surfaces of the particles. This distance h_{ij} is described as:

$$h_{ij} = R_i + R_j - \left| \boldsymbol{r}_{ij} \right| \tag{15}$$

$$\boldsymbol{r}_{ij} = \boldsymbol{r}_i - \boldsymbol{r}_j \tag{16}$$

where $\boldsymbol{r}_{ij}$ is the distance between the center of the two interacting particles i and j.

The liquid loading level Λ is expressed as in Wu et al. [24], with the half liquid bridge volume V_b normalized with the particle volume:

$$\Lambda = \frac{V_b}{2 \, V_p} \tag{17}$$

2.2.1. Liquid bridge filling model

Wu et al. [24] presented a dynamic liquid bridge filling model based on their previous work [23]. This model will be used to describe the liquid bridge formation, which is decisive for capillary and viscous forces in the system. The dimensionless forms of the mass balance differential equations are:

$$\frac{dL^*_{p,i}}{dt^*} = -a_i \left(L^*_{p,i}\, \phi_{m,i} - \frac{V^*_b}{2}\right) \tag{18}$$

$$\frac{dL^*_{p,j}}{dt^*} = -a_i \left(L^*_{p,j}\, \phi_{m,j} - \frac{V^*_b}{2}\right) \tag{19}$$

$$\frac{dV^*_b}{dt^*} = -\left(\frac{dL^*_{p,i}}{dt^*} + \frac{dL^*_{p,j}}{dt^*}\right) \tag{20}$$

$L^*_{p,i}$ and $L^*_{p,j}$ are the liquid contents on particles i and j, a_i is a dimensionless filling rate coefficient. $\phi_{m,i}$ and $\phi_{m,j}$ are the mobility coefficients of the liquid on the particle, i.e., the relative amount of liquid that is able to flow into the liquid bridge region. The dimensionless bridge volume V^*_b is defined as V_b/R^3. Based on the assumption of uniformly coated particles of equal size the mobility coefficient is determined as [24]:

$$\phi_{m,i} = \phi_{m,j} = 5\, h^*_0 \tag{21}$$

h^*_0, which represents the initial dimensionless film height, is the ratio of the actual film height h_0 and the particle radius. The following relations are used to create the dimensionless parameters:

$$L^*_{p,i} = \frac{L_{p,i}}{R^3}\,, L^*_{p,j} = \frac{L_{p,j}}{R^3}\,, t_{ref} = \frac{d_p \cdot \mu_l}{(2\,\gamma)}\,, t^* = \frac{t}{t_{ref}} \tag{22),(23),(24),(25}$$

γ is the surface tension, R the particle radius, and μ_l the liquid viscosity. The initial bridge volume $V^*_{b,0}$, will be calculated using the case of zero separation with $V^*_{b,0} = 10.5\,(h^*_0)^{1.5}$. These dimensionless parameters will remain invariant when using coarse graining.

2.2.2. Bridge rupturing model

If the critical distance between two particles is exceeded, the liquid bridge ruptures and the liquid contained in the bridge is redistributed. Wu et al. [24] assumed an equal redistribution to the two involved particles, the same assumption is made in this study. Based on Lian et al. [21] the rupture distance is represented by:

$$h_{rup} = (1 + 0.5\,\theta)\,V_b^{1/3} \tag{26}$$

h_{rup} is the critical rupture distance, and θ is the contact angle of the liquid bridge. The assumption of fully wetted particles was made in Wu et al. [24], which leads to a situation that is best approximated by assuming zero contact angle. The liquid bridge model of the present study is based on these findings and the contact angle will also be approximated as zero. As a consequence, the rupture distance is:

$$h_{rup} = V_b^{1/3} \tag{27}$$

Using the dimensionless liquid bridge volume V_b^* will lead to the dimensionless rupture distance h_{rup}^*. Both dimensionless parameters will remain invariant for the scaled and the unscaled system. Therefore, the rupture distance h_{rup} will be scaled with the coarse-graining ratio cg.

2.2.3. Capillary force model

The capillary force model is provided by Mikami et al. [19]. The capillary force is calculated from:

$$\boldsymbol{F}_{cap} = \pi\,R\,\gamma\,[\exp(\mathrm{A}\,D^* + \mathrm{B}) + \mathrm{C}]\,\boldsymbol{n}_{ij} \tag{28}$$

$$A = -1.1\,(V_b^*)^{-0.53} \tag{29}$$

$$B = [-0.34\,\ln(V_b^*) - 0.96]\cdot\theta^2 - 0.019\,\ln(V_b^*) + 0.48 \tag{30}$$

$$C = 0.0042\,\ln(V_b^*) + 0.078 \tag{31}$$

where the dimensionless surface-surface separation distance is defined as $D^* = {h_{ij}}/{R}$, with the reference length being the particle radius R. For equal-sized particles, the reference radius is simply the particle radius. If particles overlap in a collision, the dimensionless separation distance is set to zero, in that case only the parameters B and C have an impact on the capillary force calculation.

2.2.4. Viscous force model

The viscous force model by Pitois et al. [20] is used the present work:

$$\boldsymbol{F}_{vis} = -\frac{3\,\pi}{2}\,\mu_l\,\frac{R}{D^*}\,\boldsymbol{v}_{n,0}\,X_v^2\,\boldsymbol{n}_{ij} \tag{32}$$

$$X_v = 1 - \frac{1}{\sqrt{1 + \dfrac{2\,V_b^*}{\pi\,D^{*2}}}} \tag{33}$$

In the case of zero separation, the dimensionless separation is substituted by $D^* = {h_{\varepsilon,eff}}/{R}$, where $h_{\varepsilon,eff}$ is an effective roughness length of the particle. The effective roughness is the sum of the absolute roughness h_ε and the dimensionless roughness h_ε^* times the effective particle radius. For that reason, the dimensionless roughness will remain invariant when scaling the system.

2.3. Drag-force model

Beetstra et al. [39] investigated the drag force acting on particles of intermediate Reynolds number flow. For monodisperse systems the following correlation was proposed by them:

$$\boldsymbol{F}_{drag,g\to p} = \frac{18\,\mu_g\,|\boldsymbol{u}-\boldsymbol{v}|\,V_p}{d_p^2}\,(1-\phi_p)\left[\frac{10\,\phi_p}{(1-\phi_p)^2}+(1-\phi_p^2)\left(1+1.5\phi_p^{0.5}\right)\right. \tag{34}$$
$$\left.+\frac{0.413\,Re_p}{24\,(1-\phi_p)^2}\left(\frac{(1-\phi_p)^{-1}+3\,\phi_p(1-\phi_p)+8.4\,Re_p^{-0.343}}{1+10^{3\phi_p}\,Re_p^{-(1+4\phi_p)/2}}\right)\right].$$

ϕ_p is the solids volume fraction, μ_g is the gas viscosity, V_p is the particle volume and the particle Reynolds number is defined as:

$$Re_p = \frac{\rho_g\,d_p\,|\boldsymbol{u}-\boldsymbol{v}|\,(1-\phi_p)}{\mu_g} \tag{35}$$

where $\boldsymbol{u}$ is the gas velocity, $\boldsymbol{v}$ is the particle velocity, and ρ_g is the gas density.

2.4. Boundary and initial conditions

The reference impact velocity of the particles $\boldsymbol{v}_{n,0} = 1$ [m/s] is set as invariant for all test simulations. To guarantee that the particle overlap is not excessively large, the particle stiffness is derived from a fixed (desired) maximum dimensionless overlap. This dimensionless maximum overlap is set at 1 [%]. In the case only the cohesion force is considered in the analysis of the overlap, particles would overlap more than 1 [%] in case of low Bond number flows. This is simply because particle interaction forces are dominated by the gravitational force in this case. Therefore, the gravitational force will be taken into account in the determination of the particle stiffness to match the desired overlap (for further information see Appendix A.2).

The parameters were tested in a simulation of a binary collision. When setting the dimensionless filling rate coefficient equal to 0.005, the dynamic liquid bridge filling caused significantly higher overlaps (see Appendix A.2). For that reason, the dimensionless filling rate coefficient will be set to 0 in further simulations. That means no additional liquid is added to the bridge, only the liquid on the particles is distributed. Particle–wall interactions are taken into account in all performed simulations.

3. Theoretical Analysis of Coarse-Graining Strategies

In the parcel approach, the diameter of the parcel is defined via the scaling ratio cg according to $d_{parcel} = cg \cdot d_{prim}$. Consequently, one parcel consists of cg^3 particles. A coarse-graining strategy provides scaling rules for the parameters (e.g., the surface tension) used in relevant closures (e.g., for inter-particle forces). Next, a simple time scale analysis is presented, followed by a set of options for such coarse-graining strategies.

3.1. Simple time scale analysis

To be able to reproduce the behavior of the original system with coarsened particles, the time scales of the different equations need to be aligned. The dimensionless scaled time of the differential equation based on the kinematics of a simple normal head-on collision is:

$$t^*_{overlap} = \frac{t\, v_{n,0}}{R_i} \tag{36}$$

Considering the differential equation for the dynamic liquid bridge another option for the scaling of the time is:

$$t^*_{bridge} = \frac{t\, \gamma}{R_i\, \mu_l} \tag{37}$$

The ratio of the two time scales is:

$$\frac{t^*_{bridge}}{t^*_{overlap}} = \frac{v_{n,0}\ \mu_l}{\gamma} \tag{38}$$

This means the ratio of the impact velocity $v_{n,0}$ to capillary velocity γ/μ_l in case of Bond scaling needs to be constant. For a constant impact velocity, the capillary velocity must also be constant.

3.2. Contact force-based scaling for noncohesive systems

For noncohesive systems, the differential equation for the overlap in a normal direction from Newton's equation of motion is [26]:

$$m_{eff}\, \ddot{\delta}_n = k_n\, \delta_n - c_n\, \dot{\delta}_n \tag{39}$$

The effective mass and effective radius are (considering parameter $\beta = R_j/R_i$):

$$m_{eff} = \frac{m_i\, m_j}{(m_i + m_j)} = \frac{4\,\pi\, R_i^3\, \rho_P\, \beta^3}{3\,(1+\beta^3)}\,, R_{eff} = \frac{R_i\, \beta}{1+\beta} \tag{40),(41}$$

Indices i and j represent particle i and particle j respectively, which are interacting. Radl et al. [26] inserted these expressions and the dimensionless variables $\delta_n^* = \delta_n \,/\, R_i$, $\dot{\delta}_n^* = \dot{\delta}_n \,/\, v_0$, and $t^* = t\, v_0 \,/\, R_i$ with the reference velocity v_0 in Equation 39, (considering $K_1 = 4\,\pi\ \beta^3/[3\ (1+\beta^3)]$) to arrive at:

$$K_1\ \ddot{\delta}_n^* = \frac{k_n\ \delta_n^*}{R_i\ \rho_P\ v_0^2} + \frac{c_n\ \dot{\delta}_n^*}{R_i^2\ \rho_P\ v_0} \tag{42}$$

This scaling is based on the dimensionless normal overlap for the translational motion of a particle. As reference length in the parcel approach the parcel diameter is used and in the original case, the primary particle diameter is used. Therefore, the relative overlap will remain invariant when scaling the system. Based on the dimensionless differential equation for the normal overlap, the following dimensionless parameters can be identified:

$$\Pi_1 = \beta, \Pi_2 = k_n/(R_i\ \rho_P\ v_0^2),\ \Pi_3 = c_n/(R_i^2\ \rho_P\ v_0)$$

$$\Pi_{1,prim} = \Pi_{1,parcel},\ \Pi_{2,prim} = \Pi_{2,parcel},\ \Pi_{3,prim} = \Pi_{3,parcel}$$

Π_1 requires a constant ratio of the radii of the colliding parcels or particles. As long as each parcel is made up of the same number of particles N the ratio will remain constant. The parcels will be made up by a constant number of particles with the same size and the same density. As a consequence, the parcel density will be the same as the particle density. Because the reference velocity v_0 will be invariant, condition Π_2 requires that $k_n/R_i = \text{constant}$. This leads, when scaling the system, to:

$$\frac{k_{n,prim}}{R_{prim}} = \frac{k_{n,parcel}}{R_{parcel}} \tag{43}$$

Dimensionless parameter Π_3 requires that $c_n/R_i^2 = \text{constant}$, that means the damping coefficient of the primary particles c_n scales with cg^2 into the parcel system (see equation 44).

$$\frac{c_{n,prim}}{R_{prim}^2} = \frac{c_{n,parcel}}{R_{parcel}^2} \tag{44}$$

This will result in an invariant coefficient of restitution and a damping force that will scale with cg^2. When scaling the system, the dimensionless friction coefficients μ and μ_r must be kept constant [26].

3.3. Contact force-based scaling for cohesive systems

In the cohesive case, the cohesive force acts like an additional damping term:

$$m_{eff}\,\ddot{\delta}_n = k_n\,\delta_n - c_n\,\dot{\delta}_n - F_{coh} \tag{45}$$

When converting this equation to a dimensionless form, similar to the noncohesive case, an additional dimensionless parameter is obtained:

$$\Pi_4 = F_{coh}/(R_i^2\,\rho_P\,v_0^2) \tag{46}$$

For a constant dimensionless bridge volume and a constant dimensionless separation distance, this leads to:

$$\frac{\gamma_{prim}}{R_{prim}} = \frac{\gamma_{parcel}}{R_{parcel}}, \frac{\mu_{l,prim}}{R_{prim}} = \frac{\mu_{l,parcel}}{R_{parcel}} \tag{47),(48}$$

The scaling rules for the normal stiffness and normal damping coefficient remain the same for cohesive and noncohesive systems.

3.4. Stress-based scaling for cohesive systems

Bierwisch et al. [31] considered a stress-based scaling having powder filling into cavities in mind. Specifically, they assumed that the ratio of a typical cohesive stress and a hydrostatic stress remain constant in the case of coarse-graining.

In the case of stress-based scaling, obviously the ratio $Force/R_i^2$ must remain constant. For the normal stress, and in case of a constant dimensionless overlap, this leads to:

$$\frac{k_{n,prim}}{R_{prim}} = \frac{k_{n,parcel}}{R_{parcel}}, \frac{c_{n,prim}}{R_{prim}^2} = \frac{c_{n,parcel}}{R_{parcel}^2} \tag{49),(50}$$

The normal stiffness scales with cg and the normal damping factor scales with cg^2. For the capillary stress and the viscous stress, as well as a constant dimensionless bridge volume, the following scaling rules can be distilled:

$$\frac{\gamma_{prim}}{R_{prim}} = \frac{\gamma_{parcel}}{R_{parcel}}, \frac{\mu_{l,prim}}{R_{prim}} = \frac{\mu_{l,parcel}}{R_{parcel}} \tag{51),(52}$$

That means that the surface tension and liquid viscosity scale with cg. These findings are similar to the force-based scaling results.

Note that in the inertial flow regime, stress-based scaling leads to an overprediction of stresses [26]. This is because the dimensionless shear rate is increased when using parcels instead of the original particles. Unfortunately, it is not straightforward to overcome the stress overprediction in the inertial flow regime, even for dry systems.

3.5. Bond number-based scaling for cohesive systems

The cohesive influence on the system is governed by the following dimensionless parameters:

$$Bo = \frac{6\,\gamma}{d_p^2\,g\,\rho_p} \tag{53}$$

$$Ca = \frac{\mu_l\,v_t}{\gamma} \tag{54}$$

The scaling for a constant Bond number leads to:

$$\frac{\gamma_{prim}}{R_{prim}^2} = \frac{\gamma_{parcel}}{R_{parcel}^2} \tag{55}$$

Therefore, the surface tension scales with cg^2 for the sedimentation of particles. The scaling for a constant Capillary number yields:

$$\frac{\mu_{l,prim}}{\gamma_{prim}} = \frac{\mu_{l,parcel}}{\gamma_{parcel}}\,,\frac{\mu_{l,prim}}{R_{prim}^2} = \frac{\mu_{l,parcel}}{R_{parcel}^2} \tag{56),(57}$$

The liquid viscosity in this case also scales with cg^2.

In the case of Bond number-based scaling, the maximum dimensionless overlap will also be held constant. The normal stiffness in this approach is calculated via:

$$k_n = \frac{F_{coh}}{\delta_{n,max}^*\,R_i} \tag{58}$$

Rearranging this equation leads to:

$$\delta_{n,max}^* = \frac{F_{coh,prim}}{k_{n,prim}\,R_{prim}} = \frac{F_{coh,parcel}}{k_{n,parcel}\,R_{parcel}} \tag{59}$$

With the previously shown scaling rules for the surface tension and the liquid viscosity, this leads to:

$$\frac{\mathrm{k}_{n,prim}}{R_{prim}^2} = \frac{\mathrm{k}_{n,parcel}}{R_{parcel}^2} \tag{60}$$

As can be seen, the normal stiffness scales with cg^2. This nonlinear increase of the particle stiffness will require smaller simulation time steps compared with the stress scaling.

Finally, one is interested in the scaling rule for the damping coefficient. The normal damping coefficient in the Hooke contact model in LIGGGHTS® is calculated via:

$$\mathrm{c_n} = \sqrt{\frac{4\,\mathrm{m_{eff}}\,\mathrm{k_n}}{1+\left(\frac{\pi}{\ln(\mathrm{e_n})}\right)^2}} \tag{61}$$

For a constant coefficient of restitution, e_n, and where the effective mass ratio of the primary particle to the parcel being $m_{eff,prim}/m_{eff,parcel} = \left(R_{prim}/R_{parcel}\right)^3$, the scaling rule for the normal damping coefficient is:

$$\frac{c_{n,prim}}{c_{n,parcel}} = \sqrt{\left(\frac{R_{prim}}{R_{parcel}}\right)^5} \tag{62}$$

3.6. Coefficient of restitution-based scaling

Hrenya et al. [40] showed that for dilute cohesive systems considering the energy dissipated during binary collisions yields adequate scaling rules. Specifically, in case the coefficient of restitution should be unaffected by coarse-graining, the energy dissipation rate per volume and time of the original system is preserved [26,31].

The coefficient of restitution will be held constant during the collision of wet particles and the collision velocity is also constant. Therefore, the energy dissipation (for a constant dimensionless bridge volume) during the collision until reaching the bridge rupture distance is calculated. Energy gain during particle approximation will be neglected. The dissipated energy ΔE_{kin} in a binary collision, where $\dot{h}_{ij}^b$ and $\dot{h}_{ij}^a$ are the normal components of the relative velocity before and after the collision, is [31]:

$$\Delta E_{kin} = \frac{m_{eff}}{2}\left[\left(\dot{h}_{ij}^b\right)^2 - \left(\dot{h}_{ij}^a\right)^2\right] \tag{63}$$

h_{ij} is the distance between the surfaces of the particles. The overall (or "wet") coefficient of restitution $e_{n,wet}$ is expressed as [41]:

$$e_{n,wet} = \sqrt{1 - \frac{L_{t,max}}{m\ {v_{n,0}}^2}} \tag{64}$$

where $v_{n,0}$ is the initial velocity before impact. The maximal possible energy dissipation $L_{t,max}$ is:

$$L_{t,max} = 2\ (W_{vis,t} + W_{cap,t} + L_c) \tag{65}$$

$W_{vis,t}$ is the maximum possible viscous work, $W_{cap,t}$ is the maximum possible capillary work and L_c is the energy of the contact loss.

3.6.1. Capillary limiting case

For the capillary limiting case [41], the overall wet coefficient of restitution is determined from:

$$e_{n,wet} = \sqrt{1 - \frac{2\,(2\,\pi\,R\,\cos\theta\,\gamma\left(D - \sqrt{D^2 + a^2}\right) + \frac{1}{2}\,m\,(1 - e_n^2)v_{n,0}^2)}{m\,{v_{n,0}}^2}} \tag{66}$$

D is half of the separation distance h_{ij}, and the parameter a^2 is defined as:

$$a^2 = \frac{V_b}{2\,\pi\,R} \tag{67}$$

Making this so-called half-separation distance dimensionless by applying the reference particle radius yields half of the dimensionless distance D^*. Inserting these parameters and the dimensionless bridge volume V_b^* into Equation 66 leads to the dimensionless parameter:

$$\Pi_\gamma = \frac{\gamma\,\cos\theta}{R\,v_{n,0}^2\,\rho_p} \tag{68}$$

The assumption of zero contact angle and keeping the dimensionless bridge volume and the initial velocity constant leads to:

$$\frac{\gamma_{prim}}{R_{prim}} = \frac{\gamma_{parcel}}{R_{parcel}} \tag{69}$$

Thus, the surface tension should scale with cg. This is equal to the findings of the stress-based scaling.

3.6.2. Viscous limiting case

For dominant viscous effects, two dimensionless parameters characterize the system: the particle Stokes number St_v and the critical particle Stokes number $St_{v,crit}$ [41]:

$$St_v = \frac{8\,\rho_p\,v_{n,0}\,R}{9\,\mu_l}, St_{v,crit} = \left(1 + \frac{1}{e_n}\right)\ln\left(\frac{h_0}{h_{\varepsilon,avg}}\right) \tag{70),(71}$$

h_0 is the initial liquid height, and $h_{\varepsilon,avg}$ is the average surface roughness. In the critical condition (i.e., $St_v = St_{v,crit}$), the maximum possible energy dissipation in the viscous limited case is [41]:

$$L_{t,max} = \frac{3\,\pi}{2}\,R^2\,\mu_l\,u_0\left(1 + \frac{1}{e_n}\right)\ln\left(\frac{f(h_0)}{f(h_{\varepsilon,avg})}\right) \tag{72}$$

The overall wet coefficient of restitution in the viscous limiting case is:

$$e_{n,wet} = \sqrt{1 - \frac{\frac{3\,\pi}{2}\,R^2\,\mu_l\,u_0\left(1+\frac{1}{e_n}\right)\ln\left(\frac{f(h_0)}{f(h_{\varepsilon,avg})}\right)}{m\,{u_0}^2}} \tag{73}$$

With the constant dimensionless initial liquid film height $h_0^* = h_0/R$ and the constant relative roughness $h_a^* = h_a/D$, the liquid viscosity scales with:

$$\frac{\mu_{l,prim}}{R_{prim}} = \frac{\mu_{l,parcel}}{R_{parcel}} \tag{74}$$

This relation is also equal to that obtained with the stress-based scaling rules.

3.7. Drag-force scaling

The drag force in a gas–particle system is typically modeled with:

$$\boldsymbol{F}_{drag,g\to p,i} = V_{p,i}\,\beta_{p.i}\;(\boldsymbol{u}-\boldsymbol{v}) \tag{75}$$

Most of the closures for the drag coefficient $\beta_{p,i}$ can be described in the following functional form:

$$\beta_{p,i} = \frac{18\,\mu_g}{d_{p,i}^2}\left(1-\phi_p\right)\left[F_0(\phi_p)\,f(Re_p) + G_0(Re_p)\right] \tag{76}$$

The particle Reynolds number in a gas flow is given by:

$$Re_p = \frac{\rho_g\,d_{prim}\,|\boldsymbol{u}-\boldsymbol{v}|\,(1-\phi_p)}{\mu_g} \tag{77}$$

Thus, as long as the fluid-particle relative speed is kept constant, also the physical properties of the fluid (i.e., ρ_g and μ_g) must be kept invariant. This is also necessary to avoid changing fluid properties when scaling the particle system.

Another dimensionless key figure connected to a gas–particle system is the particle Froude number:

$$Fr_p = \frac{\boldsymbol{v}_t^2}{d_p\,\boldsymbol{g}} \tag{82}$$

$\boldsymbol{v}_t$ is the terminal settling velocity. Going from the original to the scaled system, the Froude number cannot be kept constant. Because if the velocities are invariant, the Froude number must change in case it is based on the parcel diameter.

4. Results for Pure Granular Flow

4.1. The Necessity of a rolling friction model

Ai et al. [38] used in their EPSD model a rolling friction coefficient of $\mu_R = 0.2$, and a viscous damping factor of $\eta_R = 0.3$. Bierwisch et al. [31] selected $\mu_R = 0.25$ for their CDT model. Similar values were tested in this work.

The simple set-up is depicted in Figure 4-1. From the initial state, the rotational speed of the particle on the top and of the one on the right is set to 20 [rad/s]. As can be seen in Figure 4-1, the use of a rolling friction model is crucial for realistic simulations. When using a no rolling friction model, single particles will keep on rolling for a long distance.

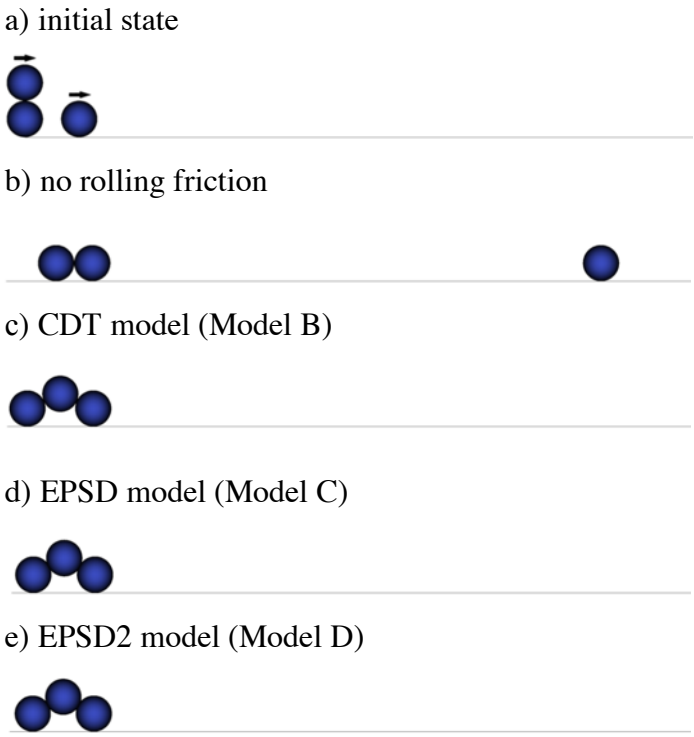

Figure 4-1: Rolling friction on a plane

From Table 4-1 can be seen that the outcome, as pictured above, for the different models is close to each other. Using no rolling friction model results in completely different behavior and data.

Table 4-1: Results of the rolling friction test

Rolling Model	μ_r (-)	η_r (-)	ke_{final} [J]	$E_{pot,final}/E_{pot,initial}$
No Roll	0.2	-	0.029	0
CDT	0.2	-	7.65e–08	0.38
EPSD	0.2	0.2	2.48e–13	0.43
EPSD2	0.2	-	9.49e–16	0.44

4.2. Coarse-graining test

As in Bierwisch et al. [31], the filling of a hopper was tested with a one-sided open box. These tests were performed as DEM simulations because potential gas–particle interactions have only an insignificant impact on the filling of a hopper for typical particles.

4.2.1. Particles with Diameter Dp = 0.05, Np = 1833 and different rolling friction models

An example of the total kinetic energy over time is displayed in Figure 4-2. Different rolling friction models were tested in this set-up because the relaxation time when the system is at rest is influenced by the rolling friction model. Therefore, the remaining rotational and translational kinetic energy of the system is compared with the gravitational potential energy of the system at the end of simulation with the so-called E ratio. If this E ratio is above 1, too much total kinetic energy exists in the system.

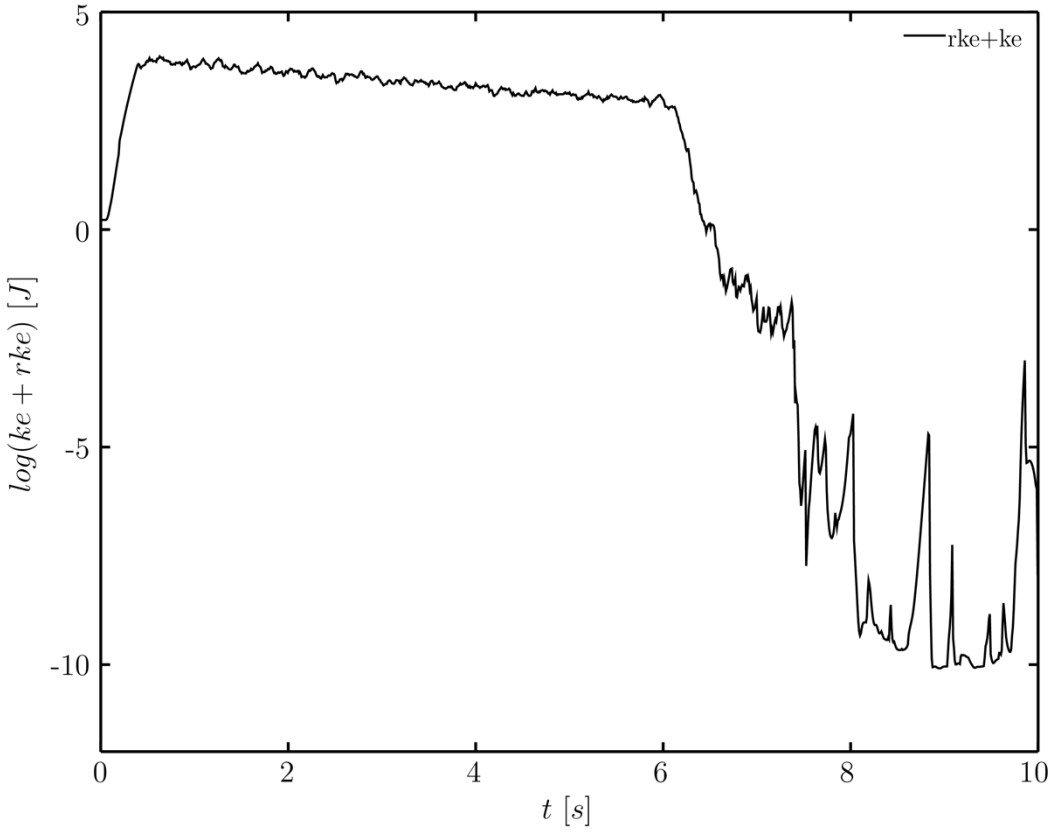

Figure 4-2: Total kinetic energy over time

As can be seen in Figure 4-3, the angle of repose is not a meaningful measurement for a cohesive system. For that reason, the ratio of the inserted particles to the remaining particles in the box was monitored. This so-called P ratio, the E ratio, and the fill level will be compared between the different simulations.

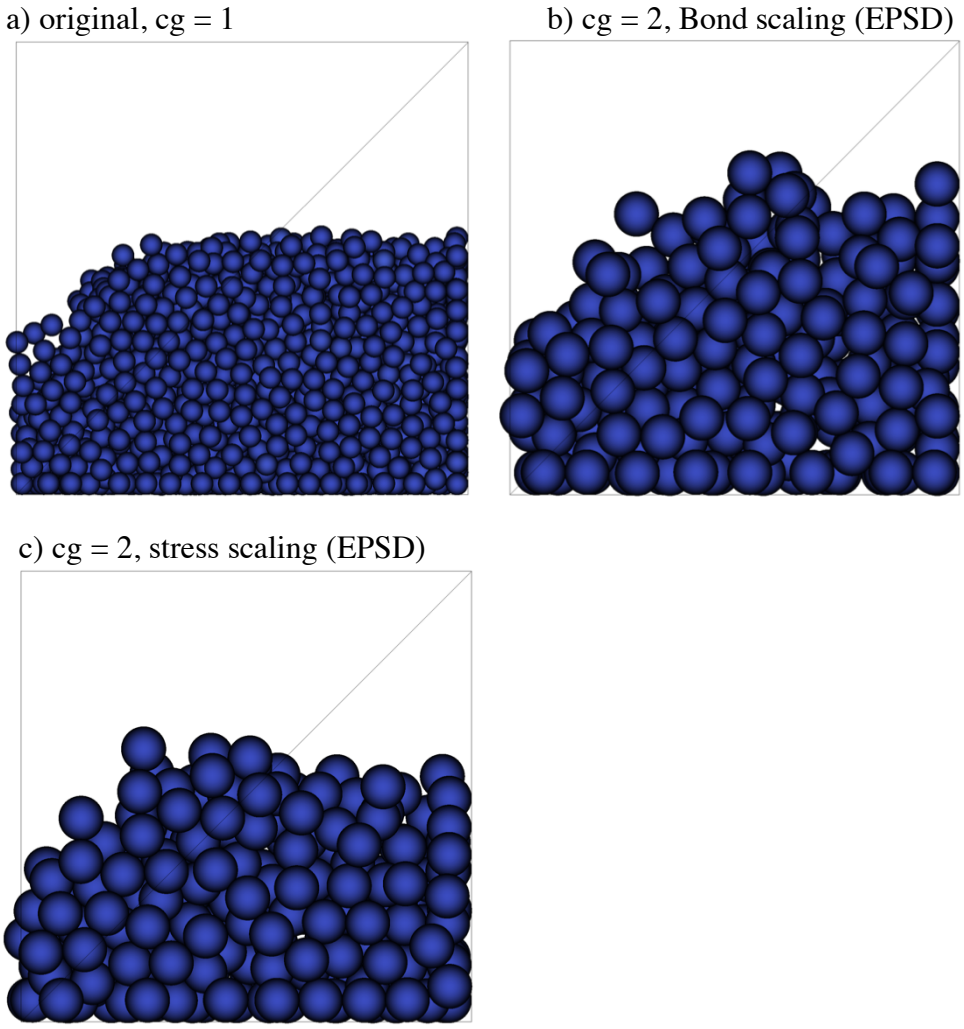

Figure 4-3: Coarse-graining test with big particles

The results of the coarse-graining test for different rolling friction models are shown in Table 4-2. For the EPSD model, both scaling strategies provide the same number of particles remaining in the box. The Bond scaling, in general, leads to more remaining particles in the system, while the stress scaling delivers variable results for different rolling friction models. As expected, the stress scaling yielded a slightly better reproduction for the P ratio of the unscaled original system.

In terms of the fill level, the outcome of the stress-scaled simulations is significantly closer to the original system than the Bond-scaling simulations. The use of the CDT model with stress scaling led to a very accurate imitation of the original system.

Table 4-2: Overview of P ratio and filling level, dp = 0.05

Model		Ins. Part.	Rem. Part.	P ratio	Dev.[%]	Fill level [m]	Dev.[%]
CDT	original,cg=1	1833	1437	78.40	-	0.5217	-
μ_r=0.2	cg=2,Bond	229	188	82.10	4.72	0.6237	19.55
	cg=2,stress	229	174	75.98	–3.09	0.5274	1.09
EPSD	original,cg=1	1833	1673	91.27		0.5464	-
μ_r=0.2	cg=2,Bond	229	217	94.76	3.82	0.6917	26.59
η_r=0.2	cg=2,stress	229	217	94.76	3.82	0.5879	7.60
EPSD2	original,cg=1	1833	1577	86.03		0.5111	-
μ_r=0.2	cg=2,Bond	229	208	90.83	5.58	0.5970	16.81
	cg=2,stress	229	199	86.90	1.01	0.5529	8.18

Table 4-3 shows the average overlap observed during the simulations. The parameters of these simulations were chosen to yield an average overlap of 1 [%]. The usage of the EPSD or EPSD2 model caused significantly higher overlaps than the usage of the CDT model. As a consequence, the CFD-DEM simulations were performed with the CDT model only.

The E ratio of the EPSD-tests is higher than the E ratio of the other tests and two times above the limit of 1. The remaining energy in the system in the case of the CDT model is significantly smaller than of the two other options.

An important objective of the coarse-graining approach is to reduce the computational cost and minimize the necessary simulation time. Overall, the coarse-graining decreased the simulation time to a large extent. The stress scaling enabled even smaller simulation times than Bond scaling because, as stated before, the Bond scaling requires an increase of the stiffness of the particles.

Table 4-3: Overview of simulation time, overlap, and E ratio, dp = 0.05

Model		Sim. time [mm:ss]	Avg. Overlap [%]	E ratio
CDT	original,cg=1	03:36	1.48	7.20e–5
μ_r=0.2	cg=2,Bond	00:15	1.25	8.50e–5
	cg=2,stress	00:10	1.78	4.00e–6
EPSD	original,cg=1	03:26	7.17	1.80
μ_r=0.2	cg=2,Bond	00:17	6.87	0.42
η_r=0.2	cg=2,stress	00:12	7.12	1.28
EPSD2	original,cg=1	03:57	6.69	0.28
μ_r=0.2	cg=2,Bond	00:17	6.36	0.49
	cg=2,stress	00:11	6.91	0.26

4.2.2. Particle with Diameter Dp = 7.5e–3, Np = 500,000

The same box with the same parameters was tested with 500,000 particles with a smaller size. The filled box for the original system and the stress-scaled systems are shown in Figure 4-4 (for the figure with the Bond-scaled set-ups see Appendix B).

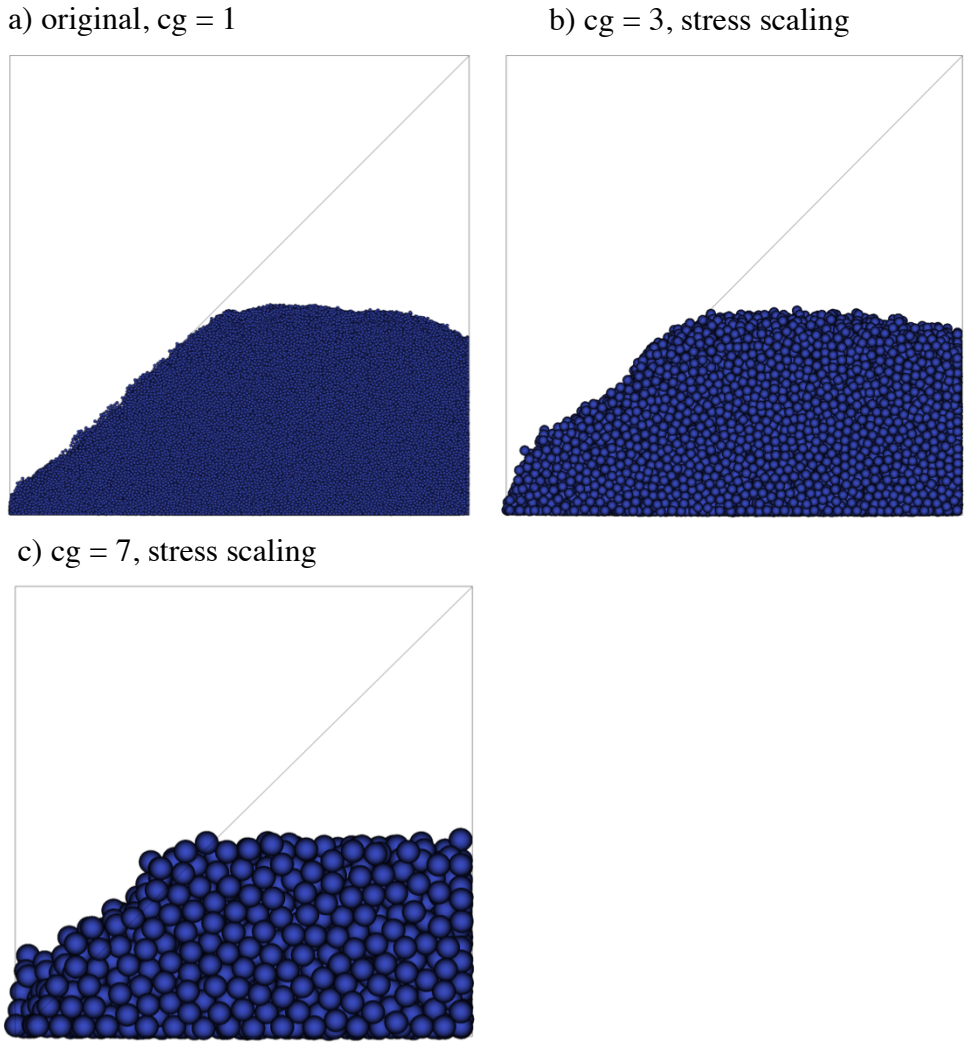

Figure 4-4: Coarse-graining test with small particles

An overview of the results is given in Table 4-4. The outcome of these simulations confirmed the findings of the test with the big particles. The stress scaling performed significantly better than the Bond scaling regarding the fill level and the P ratio.

Table 4-4: Overview of P ratio and filling level, Dp = 7.5e–3

EPSD2, μ_r=0.2	Ins. Part.	Rem. Part.	P ratio	Dev.[%]	Fill level [m]	Dev.[%]
original,cg=1	500000	387000	77.40	-	0.4260	-
cg=3,Bond	18518	15645	89.89	16.14	0.4740	11.27
cg=3,stress	18518	15115	81.62	5.45	0.4165	–2.23
cg=7,Bond	1457	1355	93.00	20.16	0.5244	23.10
cg=7,stress	1457	1241	85.18	10.05	0.4207	–1.24

An overview of the simulation time and the average overlap is given in Table 4-5. The unscaled original system was run in parallel on 16 CPUs, all other simulations on a single CPU. As can be seen, the necessary time was cut down to a very small level.

As in the simulations with the bigger particles, the E ratio of the EPSD2 model is higher for Bond scaling.

Table 4-5: Overview of simulation time, overlap, and E ratio, Dp = 7.5e–3

EPSD2, μ_r=0.2	Sim. time [hh:mm:ss]	Avg. Overlap [%]	E ratio
original,cg=1	09:19:06 (16 CPUs)	11.13	5.72e–2
cg=3,Bond	01:20:19	7.91	0.70
cg=3,stress	00:48:30	10.78	2.91e–2
cg=7,Bond	00:03:13	7.13	1.56
cg=7,stress	00:01:21	11.42	1.09e–3

Overall, the stress scaling led to a significant reduction in computational cost and still provides a reproduction of the original fill level within a deviation of 2 [%] or less.

In terms of the P ratio, deviations are smaller than 4 [%] for cg = 2, around 5 [%] for cg = 3, and 10 [%] for cg = 7. As expected for the P ratio, the differences between the coarsened and the original system increase with an increasing coarse-graining ratio.

5. Results for Fluid-Particle Suspensions

5.1. Fluidization test

The parameters of the fluidization tests are summarized in Table 5-1. The dry minimum fluidization velocity $U_{mf,dry}$ was estimated to be 0.027415 [m/s]. Girardi et al. [11] showed that a change of the fluid grid in CFD–DEM simulations causes different results. Therefore, the same CFD grid was used in all tests. For the coarsened set-ups, a smoothing algorithm was applied in case the parcel size was equal or larger than half of the fluid grid size. Specifically, a smoothing length, equal to three times the parcel diameter, was used for these smoothing operations.

Table 5-1: Parameter overview for the fluidization test

Bed size	0.009 x 0.009 x 0.18 [m]
CFD grid count	20 x 20 x 400
CFD Δgrid size	3 d_{prim}
Primary particle diameter	150e–6 [m]
Particle density	2000 [kg/m^3]
Gas density	1.25 [kg/m^3]
Gas viscosity	1.44e–5 [Pa s]
Bond number, Bo	0, 0.1, 1, 5, 10
Capillary number, Ca	0.01
Min. fluidization velocity (dry)	0.027415 [m/s]
Liquid Loading	0.001
Number of primary particles	330,024
DEM time step	5e–6 [s]
CFD time step	5e–5 [s]
Coefficient of restitution	0.4
Coefficient of friction	0.9
Coefficient of rolling friction	0.2

The superficial gas velocity was ramped from $U/U_{mf,dry} = 0$ to $U/U_{mf,dry} = 10$ in 1.5 [s]. Tests with a slower acceleration of the gas velocity were made with one-half and one-fifth of the slope (see Appendix C for results). These experiments did not cause a smaller variance of the pressure drop or less volatility of the bed height data.

In the so-called “unscaled” systems, no scaling is applied to the surface tension, liquid viscosity, or particle stiffness. Only the ratio of liquid volume to particle volume is kept constant. As a consequence, the liquid on the particle is scaled with cg^3.

The simulated pressure drop versus the superficial velocity was used to determine the fluidization point. The average pressure drop and the variance of the data after the fluidization point are used as characteristic values. In Figure 5-1, an example of this data evaluation strategy is provided.

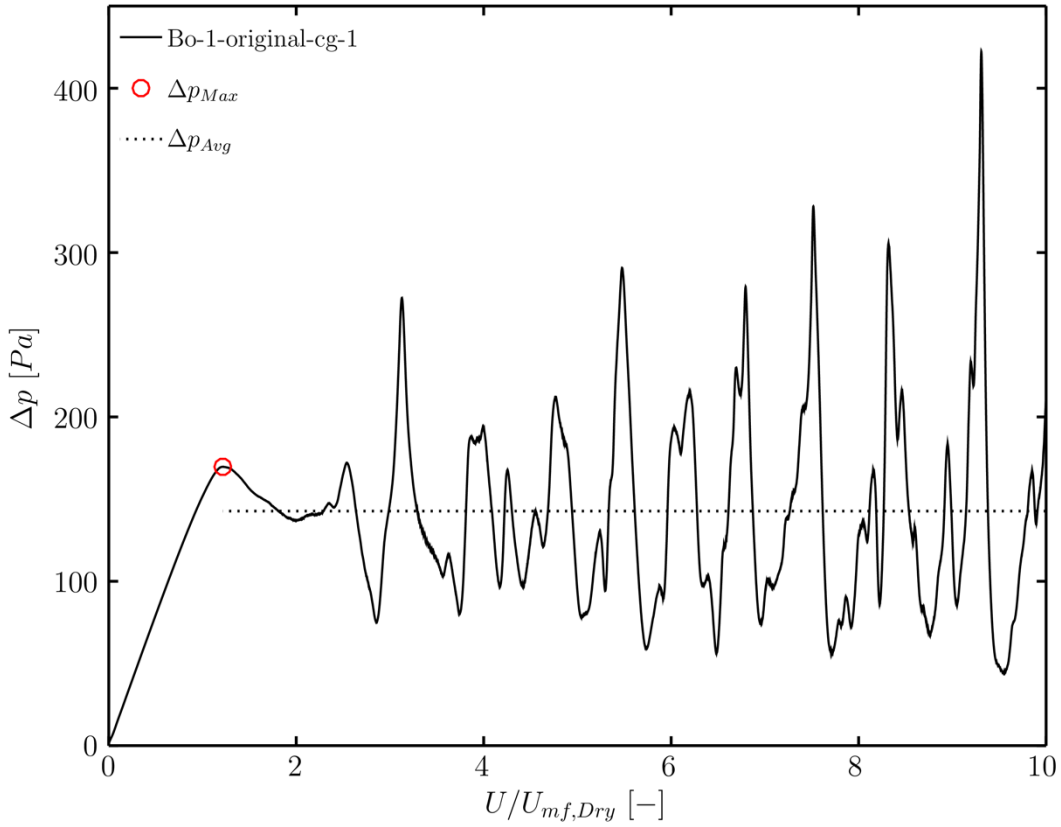

Figure 5-1: Evaluation example fluidization

The determined fluidization point was utilized for linear regression of the simulated bed height data. The slope and intersection of these regressions will be used to compare the bed behavior of different coarse-graining ratios and scaling strategies.

Boyce et al. [42] defined the bed height as the 99-quantile of all particles' heights, that means 99% of the particles are below this height. The same definition was used in the present study. The actual bed height H is divided by the initial bed height H_0 to arrive at the dimensionless bed expansion. In all simulations, the fluidized bed is filled with particles at the beginning and the fluidization starts when the bed is completely at rest.

The preliminary results indicate that the filling of the box with coarsened particles causes deviations, which range between 4 and 5 [%] in terms of the initial bed height. This needs to be considered when comparing the fluidization dynamics of the original and coarsened systems. Figure 5-2 displays an example of the linear regression and the generated bed height data.

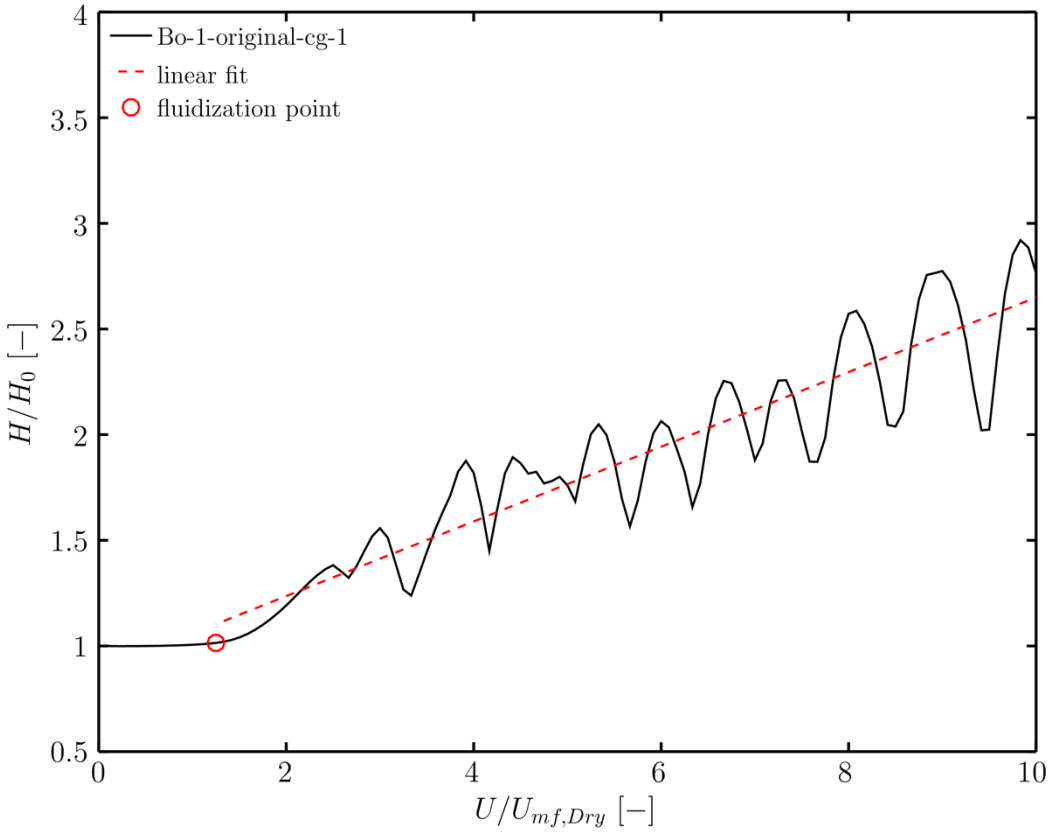

Figure 5-2: Evaluation example bed height

The maximum pressure drop for all tests is shown in Figure 5-3. As expected, the maximum pressure drop increases with an increasing Bond number. This is caused by higher cohesive forces between the particles at higher Bond numbers. In all coarse-grained systems, the pressure drop is bigger than in the original system. The overestimation of the pressure drop increases with increasing coarse-graining ratio for both scaling strategies. For Bo = 10 the unscaled system reveals the only underestimation of the maximum pressure drop.

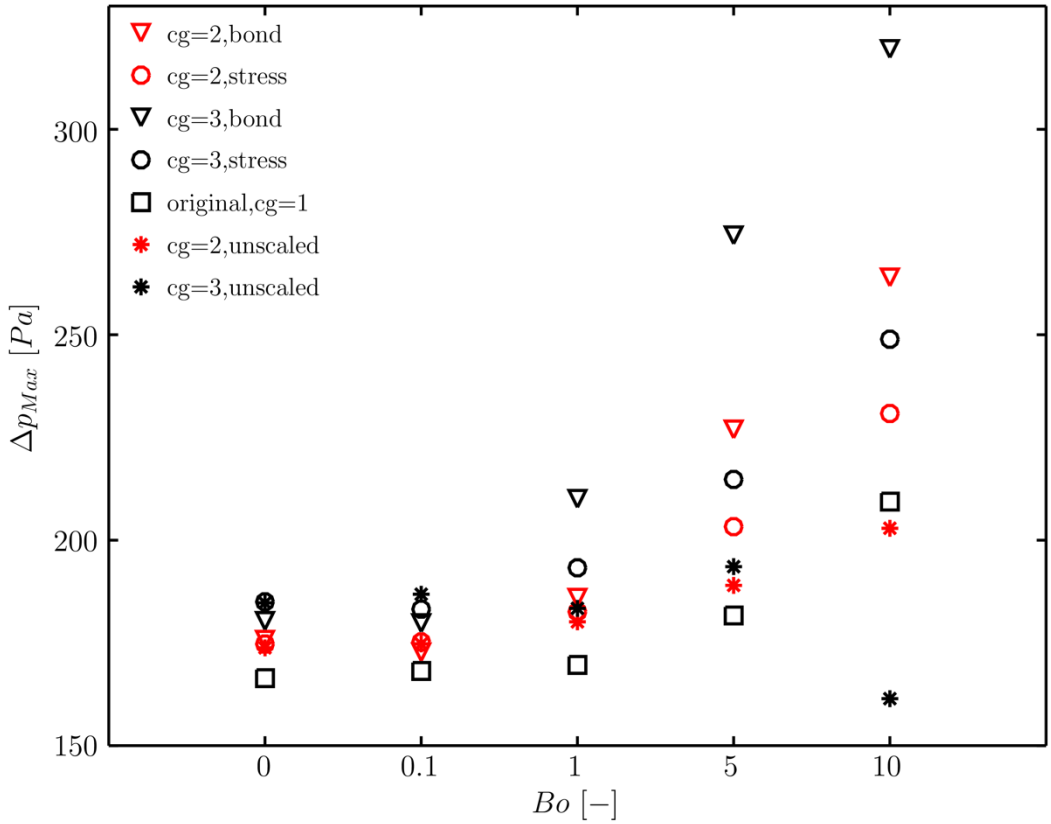

Figure 5-3: Results maximum pressure drop

The results are summarized in Table 5-2. For higher Bond numbers, the stress-scaling strategy yielded better results for cg = 2 and cg = 3 than the Bond scaling. As expected for small Bond numbers, the results are close due to the small cohesive influence.

A comparison of these results with the unscaled data shows that for noncohesive and weakly cohesive systems, the outcome is pretty close. In cohesive regions, the unscaled system yields significantly better reproduction of the original system. Because of smaller cohesive forces, the initial bed of the unscaled systems is not as compact as the bed of the scaled systems. This leads to a faster fluidization.

Table 5-2: Results maximum pressure drop

		Bo=0	Bo=0.1	Bo=1	Bo=5	Bo=10
original,cg=1	Δp_{Max} [Pa]	166.43	168.17	169.65	181.68	209.39
cg=2,Bond	Dev.[%]	5.62	2.71	9.64	24.92	26.05
cg=3,Bond	Dev.[%]	8.36	6.92	23.82	50.92	52.60
cg=2,stress	Dev.[%]	4.99	4.21	7.62	11.90	10.24
cg=3,stress	Dev.[%]	11.16	8.95	13.93	18.22	18.88
cg=2,unscaled	Dev.[%]	4.43	3.91	6.18	4.03	–3.10
cg=3,unscaled	Dev.[%]	11.01	11.11	8.11	6.54	–22.91

The average pressure drop after the fluidization point for all simulations is shown in Figure 5-4. The pressure drop for the unscaled system is higher than in the scaled systems, except for the simulations with cg = 3 and Bond scaling at Bo = 5 and Bo = 10. Up to Bo = 1, the difference of the results is again small.

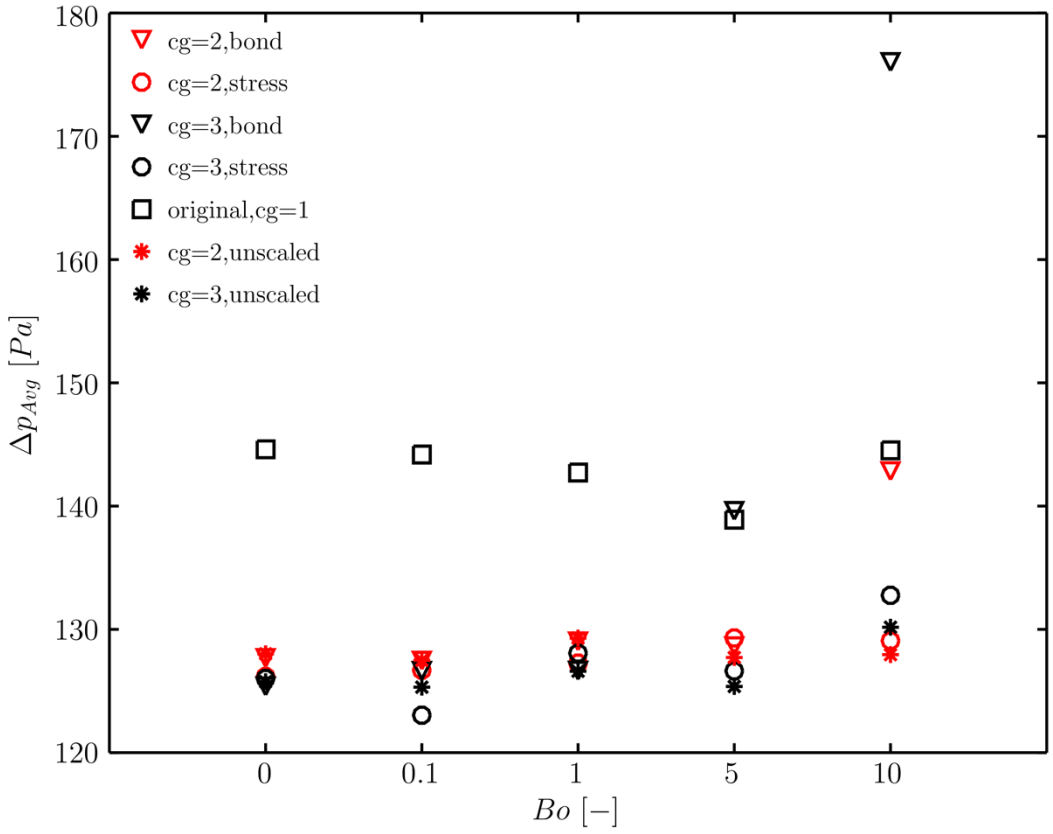

Figure 5-4: Results for average pressure drop

An overview of the results is given in Table 5-3. The deviation for the stress scaling accumulates at around –10 [%], while there are major changes of the deviation for the Bond scaling. At scaling ratio cg = 3 for Bo = 5, the prediction is very accurate and the same parameters at Bo = 10 led to the biggest deviation.

The deviation of the unscaled outcome is overall between –8 [%] and –13 [%] without big changes. As expected, the results are similar up to Bo = 1. At higher Bond numbers, the scaling of the cohesive force demonstrates a better reproduction of the original system. In the case of Bond scaling with cg = 2, the deviation decreases with increasing Bond number.

Table 5-3: Results for average pressure drop

		Bo=0	Bo=0.1	Bo=1	Bo=5	Bo=10
original,cg=1	Δp_{Avg} $[Pa]$	144.61	144.18	142.72	138.90	144.52
cg=2,Bond	Dev.[%]	–11.71	–11.60	–9.60	–7.39	–1.17
cg=3,Bond	Dev.[%]	–13.31	–12.17	–11.26	0.51	21.80
cg=2,stress	Dev.[%]	–12.75	–12.13	–10.83	–6.91	–10.69
cg=3,stress	Dev.[%]	–12.86	–14.67	–10.27	–8.83	–8.14
cg=2,unscaled	Dev.[%]	–11.47	–11.57	–9.41	–8.05	–11.47
cg=3,unscaled	Dev.[%]	–13.04	–13.09	–11.29	–9.74	–9.93

As can be seen in Figure 5-5, the variance of the original data is very high. The pressure drop of the unscaled systems fluctuates more than the scaled systems, except for the Bond scaling at cg = 3 and Bo = 10. Higher cohesive forces at higher Bond numbers lead to particle clustering. As a result, the difference of the variance between the unscaled and the scaled systems is decreasing.

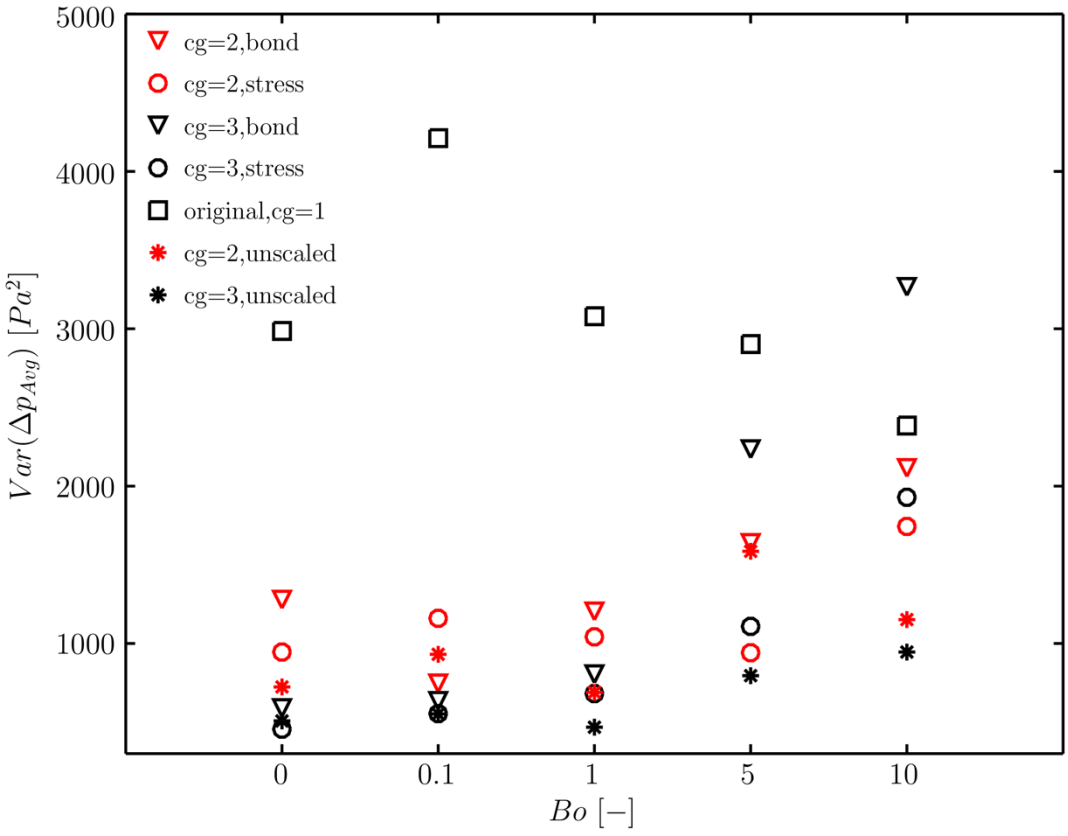

Figure 5-5: Results for the variance of the pressure drop data

For the dry system, the Bond scaling provides the best reproduction of the original system. Up to Bo = 1 the tests with cg = 2 yield better results than the simulation with cg = 3; this effect changes above Bo = 5. Table 5-4 shows the results of the

variance evaluation. Overall, the scaling of the cohesive forces reproduces the dynamics of the system after the minimum fluidization point better than the unscaled systems.

Table 5-4: Variance of the pressure drop data

		Bo=0	Bo=0.1	Bo=1	Bo=5	Bo=10
original,cg=1	$Var(\Delta p_{Avg})$ $[Pa^2]$	2986.09	4211.20	3079.56	2902.75	2384.93
cg=2,Bond	Dev.[%]	–57.20	–82.28	–60.92	–43.56	–11.32
cg=3,Bond	Dev.[%]	–80.27	–84.93	–73.88	–23.03	–36.93
cg=2,stress	Dev.[%]	–68.34	–72.45	–66.15	–67.57	–26.88
cg=3,stress	Dev.[%]	–84.74	–86.84	–77.86	–61.81	19.13
cg=2,unscaled	Dev.[%]	–75.76	–77.89	–77.62	–45.37	–51.71
cg=3,unscaled	Dev.[%]	–82.99	–86.89	–84.81	–72.60	–60.35

As displayed in Figure 5-6, higher superficial velocities are necessary for the fluidization of the coarse-grained bed. The overestimation of the wet minimum fluidization velocity increase with higher Bond numbers. Because of higher cohesive forces at higher Bond numbers, the original wet minimum fluidization velocity was expected to be higher for Bo = 10. The minimum fluidization velocity should increase with higher cohesive forces [9].

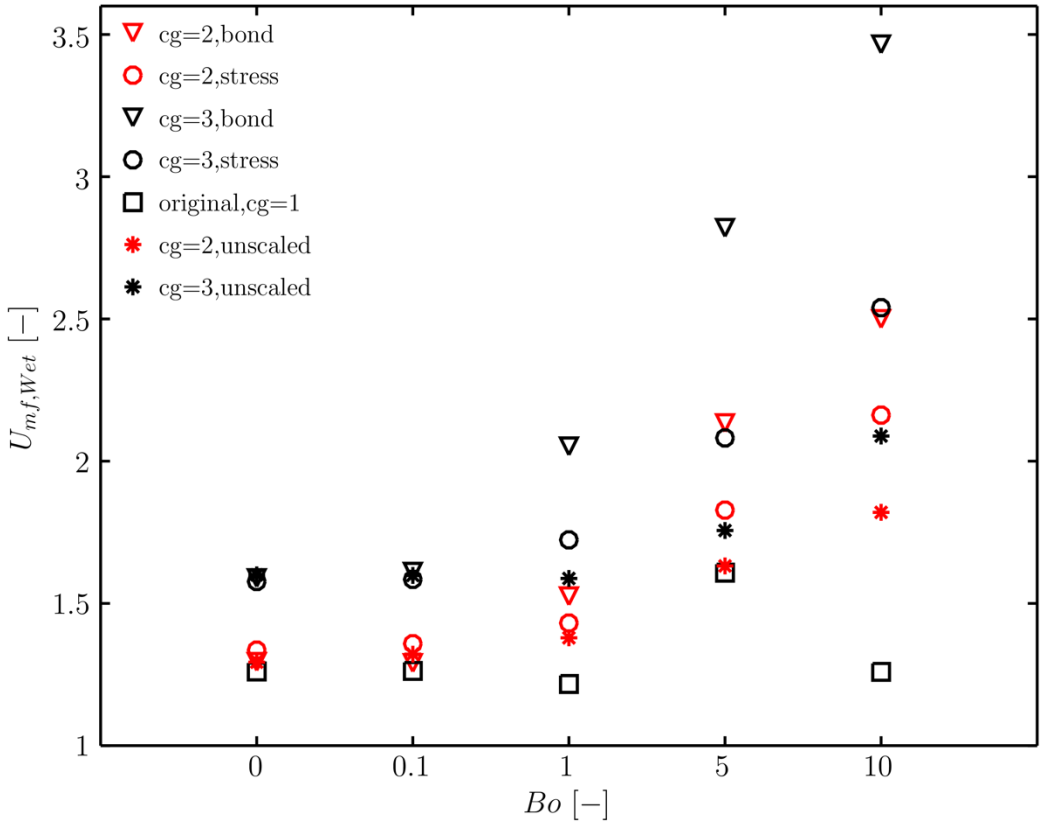

Figure 5-6: Results for minimum fluidization velocity

Table 5-5 shows that the deviation of the predicted minimum fluidization velocity for the systems with a scaling ratio of cg = 3 is higher than for systems with cg = 2. For the dry fluidization, the Bond scaling and the unscaled version yield similar results. In the case of Bo = 0.1, Bond scaling provides the best reproduction. At higher Bond numbers, the unscaled method achieved smaller deviations. This reflects the findings of the maximum pressure drop data.

Table 5-5: Results for minimum fluidization velocity

		Bo=0	Bo=0.1	Bo=1	Bo=5	Bo=10
original,cg=1	$U_{mf,Wet}$ [−]	1.26	1.26	1.22	1.61	1.26
cg=2,Bond	Dev.[%]	2.67	2.19	25.34	32.69	98.49
cg=3,Bond	Dev.[%]	26.04	27.61	68.66	75.37	175.17
cg=2,stress	Dev.[%]	5.95	7.58	17.62	13.68	71.68
cg=3,stress	Dev.[%]	25.09	25.48	41.64	29.46	101.67
cg=2,unscaled	Dev.[%]	2.59	4.67	13.34	1.47	44.52
cg=3,unscaled	Dev.[%]	26.94	26.58	30.49	9.22	65.83

In Figure 5-7 the slope of the linear fit of the bed height data is shown. In general, a bigger slope indicates a higher bed height. As can be seen, the outcome varies over the different Bond numbers.

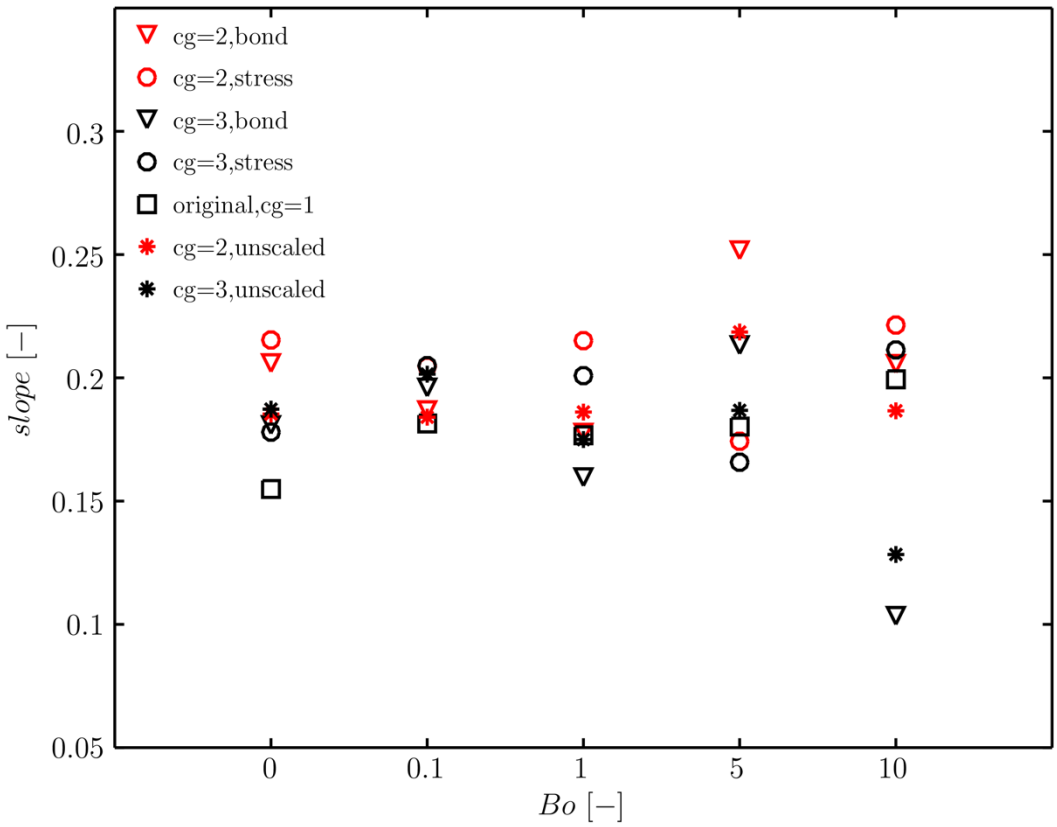

Figure 5-7: Results for the fit of bed height, slope

Table 5-6 shows that in the dry environment the test with cg = 3 shows a better or similar reproduction of the basic system than the tests with the smaller coarse-graining ratio. The Bond scaling with cg = 2 yielded a very accurate description of the original system at Bo = 0.1, Bo = 1, and Bo = 10, while the deviations for Bo = 0 and Bo = 5 shift to above 30 [%]. The unscaled results show a similar behavior over the Bond number. The stress scaling provided similar results for cg = 2 and cg = 3 at Bo = 0.1. These varying results reflect the complexity of predicting the bed height in a fluidized bed.

Table 5-6: Results for the slope linear fit

		Bo=0	Bo=0.1	Bo=1	Bo=5	Bo=10
original,cg=1	*Slope* [–]	0.155	0.182	0.177	0.180	0.199
cg=2,Bond	Dev.[%]	32.94	2.97	0.60	39.68	3.13
cg=3,Bond	Dev.[%]	16.74	8.04	–9.64	18.32	–48.13
cg=2,stress	Dev.[%]	39.01	12.80	21.74	–3.30	11.04
cg=3,stress	Dev.[%]	14.89	12.93	13.70	–8.03	5.98
cg=2,unscaled	Dev.[%]	19.62	1.41	5.34	21.28	–6.40
cg=3,unscaled	Dev.[%]	20.90	11.03	–0.98	3.65	–35.63

A snapshot for the qualitative comparison of the original system to the coarsened systems with cg = 2 is shown in Figure 5-8. As can be seen, the different coarsened set-ups led to different dynamic behavior.

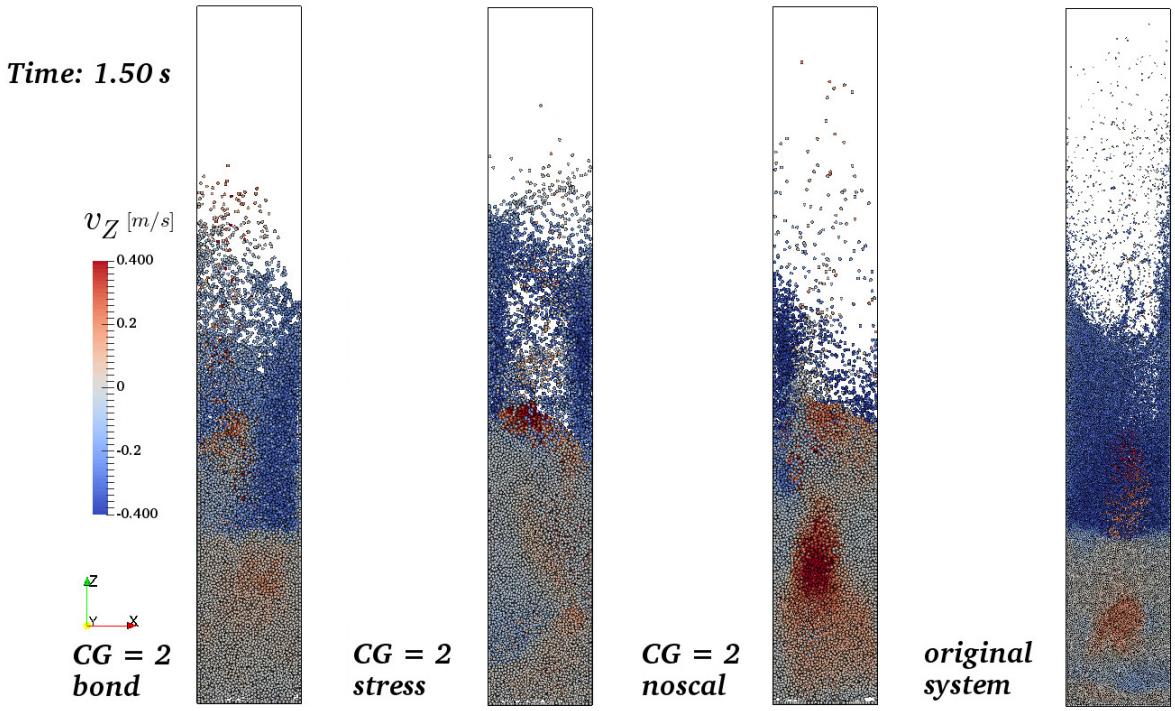

Figure 5-8: Simulation snapshot, cg = 2 at Bo = 1

The reproduction of the maximum particle height is closer with no scaling, while the closest imitation of the resting bed and the velocity of the upwards moving particles is achieved when considering the Bond scaling.

At the same time step, Figure 5-9 shows a qualitative comparison between the set-ups with cg = 3 and the original system. It can be seen that the reproduction of the system dynamics is worse for the Bond-scaled set-up compared with the set-up with cg = 2. In contrast to the Bond scaling, the outcome of the stress-scaled and the unscaled test showed improvement when increasing the coarse-graining ratio.

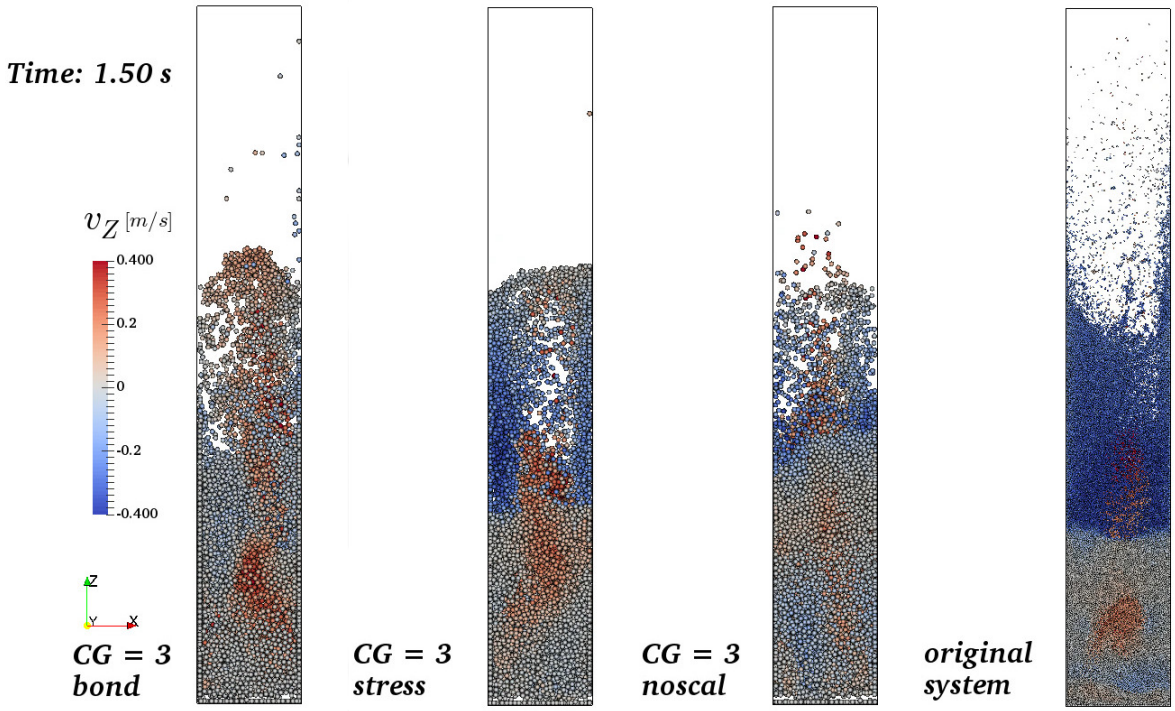

Figure 5-9: Simulation snapshot, cg = 3 at Bo = 1

The same snapshot for systems with Bo = 10 is displayed in Figure 5-10. Because of the strong cohesion, particles are partially sticking to the walls and the velocities in the bed are smaller than in the Bo = 1 set-up. This snapshot confirms the qualitative finding that the prediction of the bed height is the best with the Bond scaling for small coarse-graining ratios. The bed expansion is too small without any scaling of the cohesive forces and the velocities of the upward moving parcels are too high for the stress-scaled system.

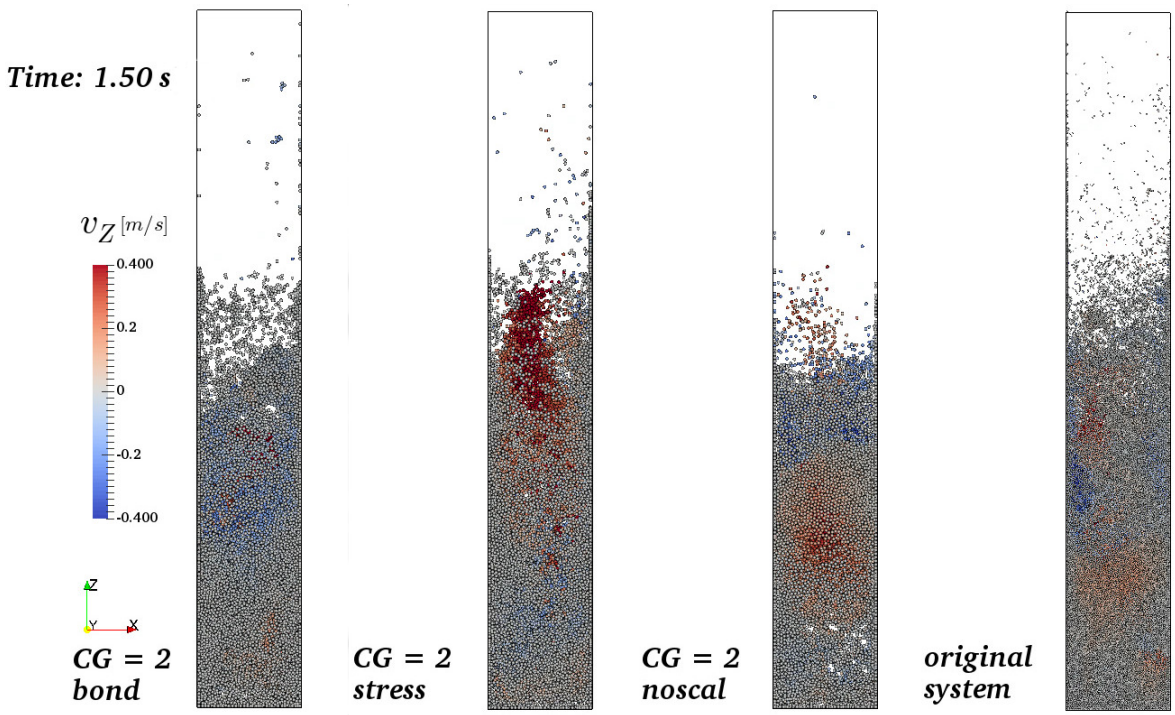

Figure 5-10: Simulation snapshot, cg = 2 at Bo = 10

As shown in Figure 5-11, the imitation of the bed expansion is worse at cg = 3 than at cg = 2, this behavior reflects the finding of the test with Bo = 1. The nonlinear scaling of the cohesive forces in the Bond-based scaling results into a single big particle cluster (at cg = 3) that heavily influences the fluidization behavior. In a quantitative view, the stress-scaling strategy demonstrated the closest reproduction of the original system for this parameter combination.

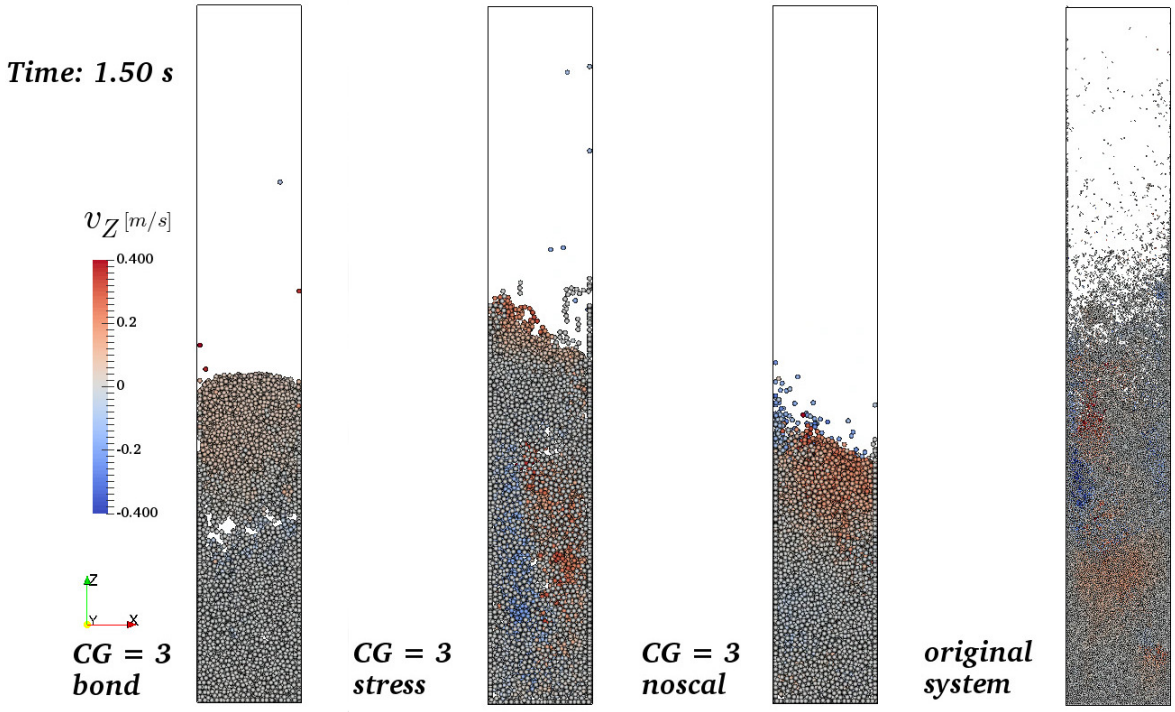

Figure 5-11: Simulation snapshot, cg = 3 at Bo = 10

However, no significant evidence was found that the scaling of the cohesive forces leads to an overall better reproduction of the original system. Because of the small cohesive influence, the results of the unscaled and scaled systems are collectively close up to Bo = 1.

Different characteristics of the fluidized bed require different scaling strategies. For example, in the case of finding the maximum pressure drop, the unscaled set-up at cg = 2 provided the best reproduction with a mean deviation of 4 [%], while the stress scaling with cg = 2 yielded an average overall deviation of 7 [%]. For the wet minimum fluidization velocity, the unscaled set-up with cg = 2 also achieved the smallest deviations accumulated around 13 [%]. In contrast to the minimum fluidization behavior, the outcome of the Bond scaling with cg = 2 showed the closest reproduction of the average pressure drop after the minimum fluidization point. The same finding is true for the variance. Both deviations decrease with an increasing Bond number. This suggests that for higher superficial velocities the Bond-based scaling strategy provides a better reproduction of the system dynamics. Between Bo = 0.1 and Bo = 1, the Bond scaling yielded the best result. However, above that the nonlinear scaling of the cohesive parameters is overpredicting the cohesive influence, especially at higher coarse-graining ratios.

The required simulation time is summarized in Table 5-7. As displayed, the simulation time was reduced by at least a factor of 4 for cg = 2 and a factor of 7 for cg = 3. As expected, the dry systems needed less simulation time.

Table 5-7: Overview of the required simulation time of the fluidization tests

Sim. Time [hh:mm:ss]					
	Bo=0	Bo=0.1	Bo=1	Bo=5	Bo=10
original,cg=1	22:25:57	31:16:23	34:12:24	32:25:31	31:27:28
cg=2,Bond	05:28:36	06:56:55	06:56:15	06:48:26	05:36:44
cg=3,Bond	03:39:02	04:47:41	04:48:29	04:35:57	04:42:38
cg=2,stress	05:24:02	07:02:15	07:05:57	05:38:12	05:36:13
cg=3,stress	03:10:54	03:53:38	03:55:04	04:34:28	04:43:13

5.2. Sedimentation in a Periodic Box

The parameters of the periodic box simulations are displayed in Table 5-8. The same particle properties as in the fluidization test are used, excluding the Young's modulus, which is set to 4e6 [Pa] for the primary particles.

Table 5-8: Parameter overview for the periodic box

Periodic Box	0.018 x 0.018 x 0.072 [m]
CFD grid count	40 x 40 x 160
CFD Δgrid size	3 d_{prim}
Primary particle diameter	150e–6 [m]
Particle density	2000 [kg/m^3]
Gas density	1.3 [kg/m^3]
Gas viscosity	1.44e–5 [Pa s]
Bond number, Bo	0, 0.1, 1, 10
Capillary number, Ca	0.01
Liquid Loading	0.001
Particle volume fraction	0.10
DEM time step	1e–6 [s]
CFD time step	1e–5 [s]
Coefficient of restitution	0.4
Coefficient of friction	0.9
Coefficient of rolling friction	0.2

The calculated terminal settling velocity $\boldsymbol{v}_t$ is 0.8562 [m/s] and the reference time is determined based on $t_{ref} = \boldsymbol{v}_t/\boldsymbol{g}$. The domain-averaged slip velocity $\langle \boldsymbol{v}_{slip} \rangle$ is calculated from $\langle \boldsymbol{u}_g \rangle - \langle \boldsymbol{v}_s \rangle$, where the domain-averaged gas velocity $\langle \boldsymbol{u}_g \rangle$ and the average solid velocity $\langle \boldsymbol{v}_s \rangle$ are:

$$\langle \boldsymbol{u}_g \rangle = \frac{1}{V_d \langle \phi_g \rangle} \int \left(\phi_g \, \boldsymbol{u}_g \right) dV \,, \qquad \langle \boldsymbol{v}_s \rangle = \frac{1}{N_p} \sum^{N_p} \boldsymbol{v}_s \tag{82),(83}$$

$\langle \boldsymbol{v}_{slip} \rangle$ is one of two important indicators in the determination of inhomogeneities in the flow structure, the other possibility is the observation of the volume fraction distribution. The simulations are performed until 40 t/t_{ref} is reached because, as shown in Figure 5-12, the flow in the periodic systems approaches a statistical steady state after approximately 5 t/t_{ref}. The mean and variance of the obtained data are calculated after stabilization in this statistical steady state. The analytic solution for the sedimentation speed of a homogeneous suspension is also displayed.

The reference momentum of the periodic simulations was compared with the total momentum. This is to achieve that the simulation runs in a stable mode. The

outcome of these tests is valid if the reference momentum is approximately two orders of magnitude higher than the total momentum, which was the case for all simulation data presented below.

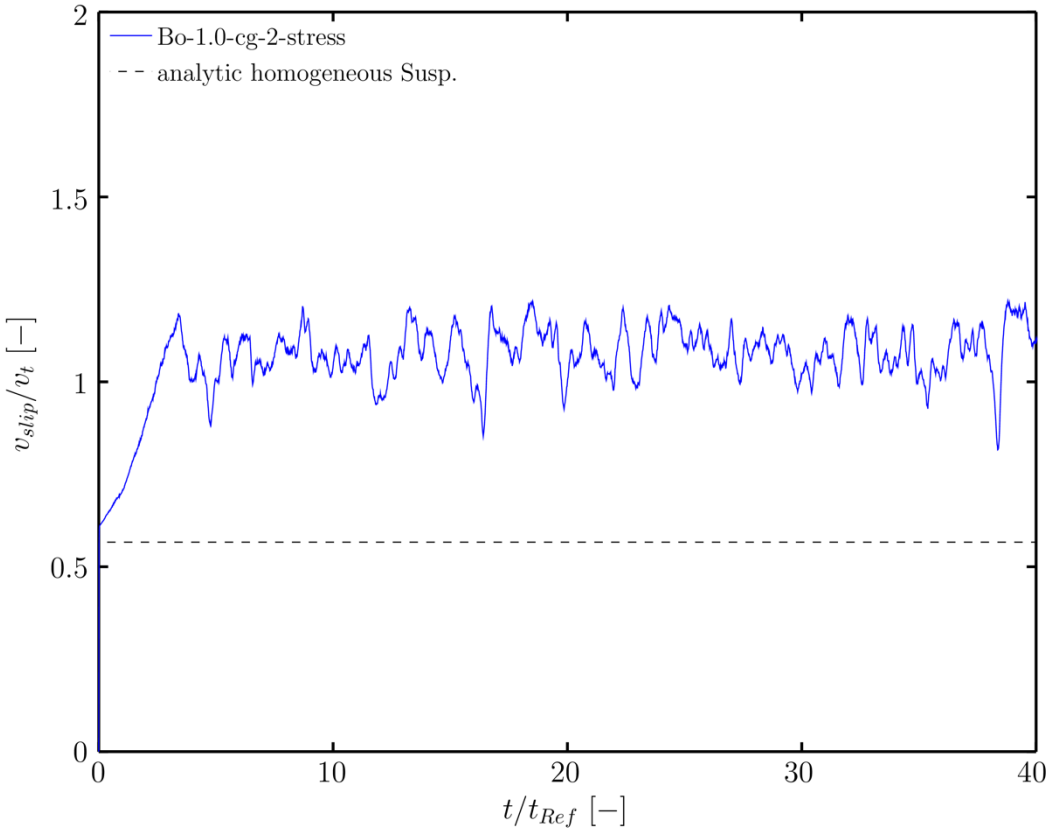

Figure 5-12: Simulation outcome example for a periodic box

In Figure 5-13, v_{slip}/v_t is shown for different Bond numbers. As can be seen, the results suggest more stable tendencies than the outcome of the fluidization test. In the literature, increasing slip velocities with increasing Bond numbers were identified [11,24]. The same trend can be found when looking at the overall tendency of the slip velocity.

The ratio of the velocities is slightly increasing over the Bond number for the stress-scaled system, while the Bond-scaled set-ups show a stronger growth going from Bo = 1 to Bo = 10. The unscaled data remain almost unchanged over the different regimes. As displayed in Figure 5-13, a higher coarse-graining ratio led to significantly smaller velocities and therefore higher deviations. This confirms the findings of the box-filling test and the fluidization test that the difference between the original and coarsened systems increases with increasing coarse-graining ratio. Up to Bo = 1, the outcomes of the unscaled and scaled set-ups are located close to

each other. At Bo = 10, a significant difference can be determined between the coarsened cases. This indicates that in more cohesive systems the scaling of the cohesive forces achieves better results than the unscaled systems.

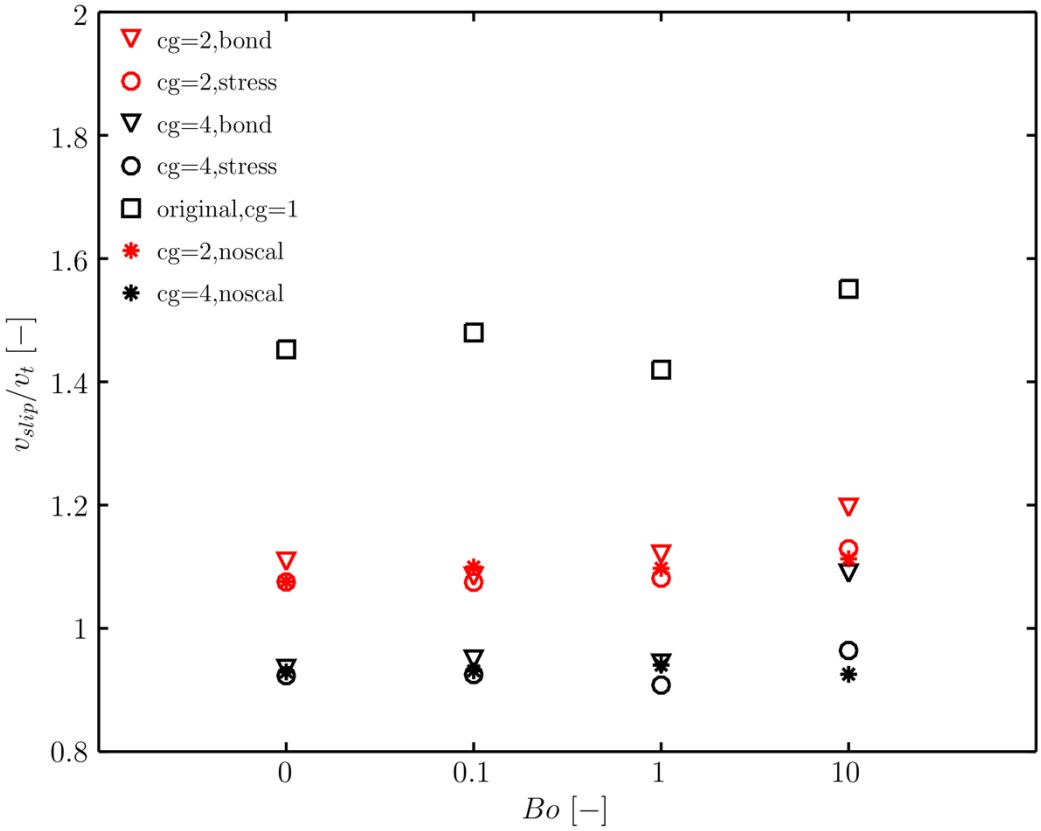

Figure 5-13: v_{slip}/v_t over different Bond numbers

An overview of the obtained data is given in Table 5-9. For Bo = 0 and Bo = 0.1, the deviations for cg = 2 accumulate around 25 [%] and for cg = 4 around 36 [%]. As expected, the influence of the scaling strategy is small in this non or midly cohesive regime. The deviations to the respective original systems are overall above 20 [%] with cg = 2 and at least 29 [%] with cg = 4. At Bo = 1, the Bond scaling yielded the closest reproduction at cg = 2 and at cg = 4. In the cohesive-dominated regime at Bo = 10, the Bond scaling provided the best imitation of the original system.

Table 5-9: Results for v_{slip}/v_t with the periodic box

		Bo=0	Bo=0.1	Bo=1	Bo=10
original,cg=1	$\langle \boldsymbol{v}_{slip} \rangle / \langle \boldsymbol{v}_t \rangle$ [-]	1.453	1.480	1.420	1.551
cg=2,Bond	Dev.[%]	–23.70	–26.74	–21.11	–22.88
cg=4,Bond	Dev.[%]	–35.67	–35.83	–33.57	–29.76
cg=2,stress	Dev.[%]	–25.98	–27.38	–23.83	–27.20
cg=4,stress	Dev.[%]	–36.45	–37.50	–36.05	–37.83
cg=2,unscaled	Dev.[%]	–26.15	–25.71	–22.71	–28.24
cg=4,unscaled	Dev.[%]	–36.03	–37.09	–33.76	–40.32

Figure 5-14 displays the obtained variance over different Bond numbers. A higher variance points out higher fluctuations of the slip velocity in the statistical steady state. As shown, the outcome varies, in contrast to the more stable tendencies of the collected mean slip velocities. At Bo = 10, the Bond-scaled set-up with cg = 4 generated the only overprediction of the variance; with cg = 2 the increase between Bo = 1 and Bo = 10 is also stronger than in the original case or in the other coarsened systems. This effect is caused by the nonlinear scaling of the cohesive parameters in the Bond-based scaling strategy, which causes bigger parcel clusters at high coarse-graining ratios.

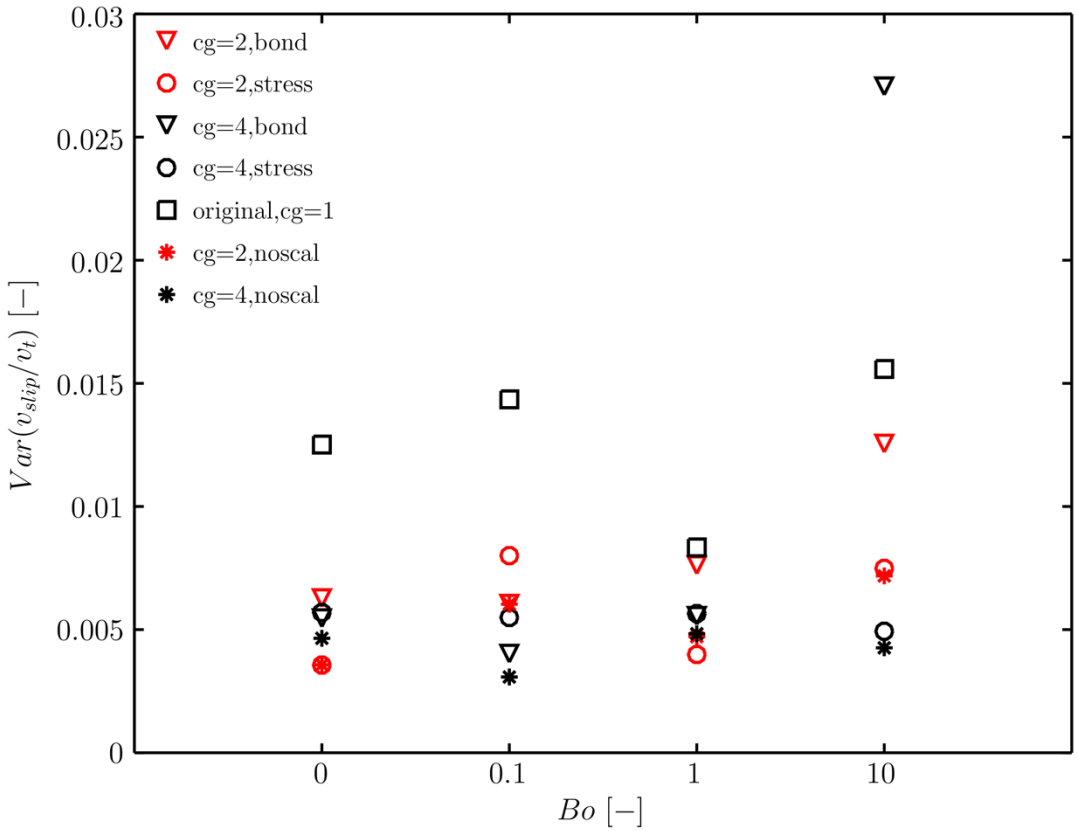

Figure 5-14: Variance over different Bond numbers

An overview of the quantitative measurements is given in Table 5-10. The unscaled set-up with cg = 2 follows the trend of the basic system, whereas at cg = 4 the tendency is the reverse of the original case. The Bond scaling with cg = 2 achieved the closest reproduction of the original system at Bo = 1 and Bo = 10.

Table 5-10: Results for the variance of the statistical steady state

		Bo=0	Bo=0.1	Bo=1	Bo=10
original,cg=1	$Var(\langle \boldsymbol{v}_{slip} \rangle / \langle \boldsymbol{v}_t \rangle)$ [-]	1.25e-02	1.44e-02	8.34e-03	1,56e-02
cg=2,Bond	Dev.[%]	–49.84	–57.86	–8.66	–19.45
cg=4,Bond	Dev.[%]	–56.34	–71.97	–33.34	73.64
cg=2,stress	Dev.[%]	–71.55	–44.22	–52.16	–51.96
cg=4,stress	Dev.[%]	–54.48	–61.72	–32.21	–68.35
cg=2,unscaled	Dev.[%]	–67.39	–57.96	–43.49	–53.91
cg=4,unscaled	Dev.[%]	–62.87	–78.57	–42.04	–72.66

A qualitative comparison of the original system at Bond numbers 0 and 10 is shown in Figure 5-15. As can be seen in the system with Bo = 10, more upward moving particles are present. One strand of upward moving particles is visible from the top to the bottom, whereas in the dry case no such structure exists.

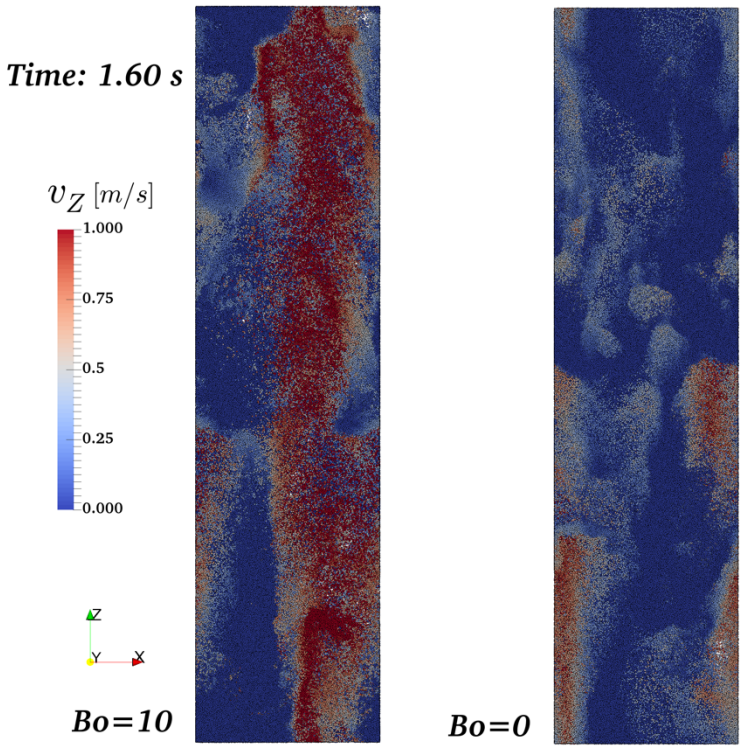

Figure 5-15: Simulation snapshot over the basic case at Bo = 0 and Bo = 10

All coarsened set-ups with cg = 2 for Bo = 10 and the original system are shown in Figure 5-16. The Bond-scaled system achieved the closest reproduction of the domain-averaged slip velocity. As shown, velocities of the particles are significantly

smaller in the coarsened system than in the basic case. More areas without particles are visible in the Bond-scaled set-up than in the other cases due to the quadratic scaling of the cohesive parameters.

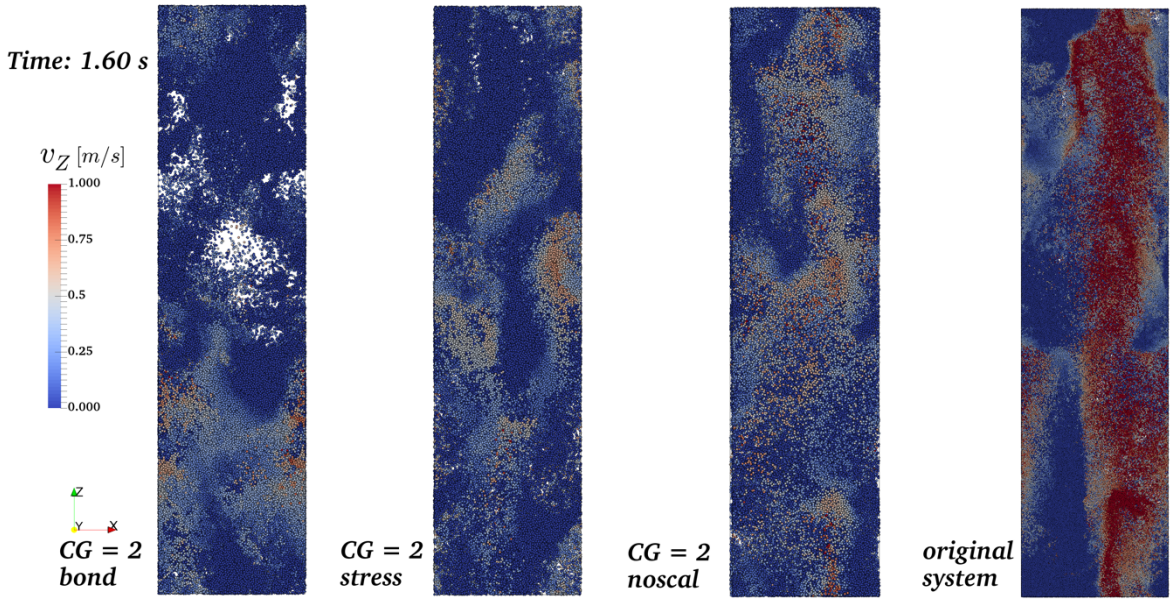

Figure 5-16: cg = 2 comparison at Bo = 10

Figure 5-17 shows the same snapshot, but for set-ups with cg = 4. The reduction from 1.3 million particles in the original system to 20627 parcels in the coarsened system is clearly visible, in particular, in the Bond-scaled system where the parcels build significantly more clusters than in the other coarsened systems.

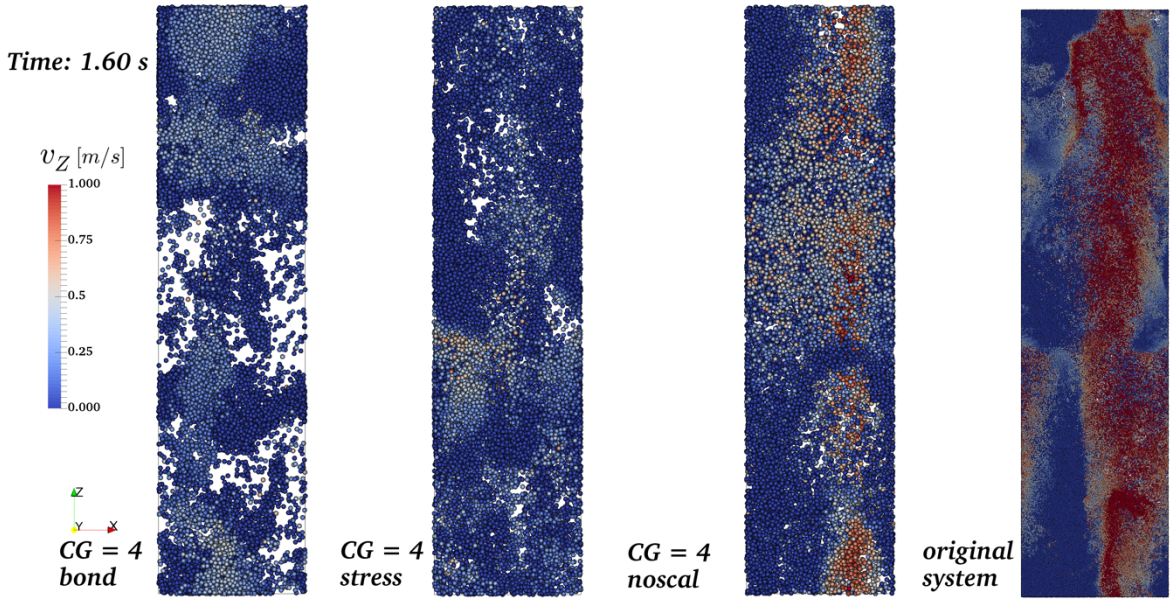

Figure 5-17: cg = 4 comparison at Bo = 10

A example of the required simulation times is shown in Table 5-11. As displayed the original system was running in parallel on 128 CPU's for around 40 days. The coarse-graining reduced the simulation time by a factor of 4 for cg = 2 and a factor of 6 for cg = 4 with half of the CPU usage.

Table 5-11: Required simulation time of periodic box tests with Bo=0.1

Sim. Time [hh:mm:ss]		
	Bo=0.1	CPU's
original,cg=1	970:13:01	128
cg=2,Bond	241:35:13	64
cg=4,Bond	160:13:37	64
cg=2,stress	246:04:30	64
cg=4,stress	163:48:16	64

6. Conclusions

This work highlighted the necessity for the implementation of rolling friction models, and their influence on DEM simulations was verified in two tests: a simple test where particles are rolling on a horizontal plane and the test of cavity filling a box with one open side.

A theoretical analysis of various coarse-graining strategies was performed and two different ways of scaling the cohesive influence, when going from the primary particles to the scaled parcels, were identified. The proposed scaling strategies were compared to an unscaled coarse-graining setup in CFD-DEM simulations of a fluidized bed, and in the simulation of the sedimentation in a periodic box. The DEM simulation of cavity filling was also used to investigate the effect of coarse-graining, and the importance of the rolling friction models.

The necessity of the implementation of a rolling friction model was verified. The use of elastic-plastic spring–dashpot models caused particle relaxation at the end of simulations, where particles should be at rest. Applying a constant directional torque model to the DEM simulations prevented these problems, although this CDT model is less realistic than the EPSD models. The stress scaling led to a very accurate imitation of the original system in the cavity-filling test even at high coarse-graining ratios and big simulations with 500,000 primary particles.

As expected for the CFD–DEM simulations, a higher coarse-graining ratio led to a higher inaccuracy in reproducing the original system. Because of the small cohesive influence up to Bo = 1, the outcomes of the unscaled and scaled systems are close; no significant improvement when scaling the cohesive forces was found in these regimes. The simulation of the fluidized bed indicates at Bo = 10 that Bond scaling with cg = 2 provided the best imitation of the bed height and the closest reproduction of the system dynamics when the bed is already fluidized. This changes at higher coarse-graining ratios where the nonlinear scaling of the cohesive parameters leads to an overprediction of the cohesive force and therefore bigger clusters. In terms of finding the maximum pressure drop and minimum fluidization velocity, the unscaled set-up yielded the best results. This indicates that the scaling of the cohesive parameters causes a higher compaction of the resting bed.

The results of the periodic box at Bo = 10 also slightly indicate that scaling of the cohesive forces leads to better results than the unscaled set-ups in already cohesive-dominated fluidized systems.

The necessary computational time could be reduced by a factor of 24 with cg = 3 and over 800 with cg = 7 in the cavity-filling DEM simulations, while deviations of the fill level with the stress-scaled set-up were under 2 [%]. In the CFD–DEM simulations in which the same fluid time step was used in different set-ups, the computational cost was cut down by at least a factor of 4 for cg = 2 and a factor of 7 for cg = 3.

For clear evidence that the scaling of the cohesive force is superior to other scaling strategies, more simulations in stronger cohesive environments need to be performed. A detailed analysis on the influence of coarse-graining wet systems on different liquid bridge models would provide new helpful insights for further improvements of the parcel-based approach. Potentially the use of more complex models when describing particle interactions or the liquid distribution could refine the imitation of original nonscaled systems.

7. References

[1] P. K. House, M. Saberian, C. L. Briens, F. Berruti, and E. Chan, "Injection of a liquid spray into a fluidized bed: Particle-liquid mixing and impact on fluid coker yields," *Ind. Eng. Chem. Res.*, vol. 43, no. 18, pp. 5663–5669, 2004.

[2] F. J. Muzzio, T. Shinbrot, and B. J. Glasser, "Powder technology in the pharmaceutical industry: The need to catch up fast," *Powder Technol.*, vol. 124, no. 1–2, pp. 1–7, 2002.

[3] B. J. Glasser, S. Sundaresan, and I. G. Kevrekidis, "From bubbles to clusters in fluidized beds," *Phys. Rev. Lett.*, vol. 81, no. 9, pp. 1849–1852, 1998.

[4] S. Sundaresan, "Instabilities in fluidized bed," *Annu. Rev. Fluid Mech.*, vol. 35, no. 1, pp. 63–88, 2003.

[5] S. Herminghaus, "Dynamics of wet granular matter," *Adv. Phys.*, vol. 54, no. 3, pp. 221–261, 2005.

[6] J. P. K. Seville and R. Clift, "The effect of thin liquid layers on fluidisation characteristics," *Powder Technol.*, vol. 37, no. 1, pp. 117–129, 1984.

[7] M. A. Mullier, J. P. K. Seville, and M. J. Adams, "A fracture mechanics approach to the breakage of particle agglomerates," *Chem. Eng. Sci.*, vol. 42, no. 4, pp. 667–677, 1987.

[8] M. L. Passos and A. S. Mujumdar, "Effect of cohesive forces on fluidized and spouted beds of wet particles," *Powder Technol.*, vol. 110, no. 3, pp. 222–238, 2000.

[9] L. J. McLaughlin and M. J. Rhodes, "Prediction of fluidized bed behaviour in the presence of liquid bridges," *Powder Technol.*, vol. 114, no. 1–3, pp. 213–223, 2001.

[10] C. Boyce, A. Ozel, J. Kolehmainen, S. Sundaresan, C. McKnight, and M. Wormsbecker, "Growth and Breakup of a Wet Agglomerate in a Dry Gas–Solid Fluidized Bed," *Am. Inst. Chem. Eng. J.*, vol. 63, no. 7, pp. 2520–2527, 2017.

[11] M. Girardi, S. Radl, and S. Sundaresan, "Simulating wet gas-solid fluidized beds using coarse-grid CFD-DEM," *Chem. Eng. Sci.*, vol. 144, pp. 224–238, 2016.

[12] S. Tenneti and S. Subramaniam, "Particle-Resolved Direct Numerical Simulation for Gas-Solid Flow Model Development," *Annu. Rev. Fluid Mech.*, vol. 46, no. 1, pp. 199–230, 2014.

[13] D. Gidaspow, *Multiphase Flow and Fluidization: Continuum and Kinetic Theory Descriptions*. Elsevier, 1994.

[14] R. Jackson, *The Dynamics of Fluidized Particles*. Cambridge University Press, 2000.

[15] N. G. Deen, M. Van Sint Annaland, M. A. Van der Hoef, and J. A. M. Kuipers, "Review of discrete particle modeling of fluidized beds," *Chem. Eng. Sci.*, vol. 62, no. 1–2, pp. 28–44, 2007.

[16] Q. F. Hou, Z. Zhou, and A. Yu, "Micromechanical modeling and analysis of different flow regimes in gas fluidization," *Chem. Eng. Sci.*, vol. 84, pp. 449–468, 2012.

[17] J. E. Galvin and S. Benyahia, "The Effect of Cohesive Forces on the Fluidization of Aeratable Powders," *AIChE J.*, vol. 60, pp. 473–484, 2014.

[18] P. Cundall and O. Strack, "A discrete numerical model for granular assemblies," *Geotechnique*, vol. 29, no. 1, pp. 47–65, 1979.

[19] T. Mikami, H. Kamiya, and M. Horio, "Numerical Simulation of Cohesive Powder Behavior in a Fluidized Bed," *Chem. Eng. Sci.*, vol. 53, no. 10, pp. 1927–1940, 1998.

[20] O. Pitois, P. Moucheront, and X. Chateau, "Liquid Bridge between Two Moving Spheres: An Experimental Study of Viscosity Effects," *J. Colloid Interface Sci.*, vol. 231, no. 1, pp. 26–31, 2000.

[21] G. Lian, C. Thornton, and M. J. Adams, "A Theoretical Study of the Liquid Bridge Forces between Two Rigid Spherical Bodies," *J. Colloid Interface Sci.*, vol. 161, pp. 138–147, 1993.

[22] D. Shi and J. J. McCarthy, “Numerical simulation of liquid transfer between particles,” *Powder Technol.*, vol. 184, no. 1, pp. 64–75, 2008.
[23] M. Wu, S. Radl, and J. G. Khinast, “A Model to Predict Liquid Bridge Formation Between Wet Particles Based on Direct Numerical Simulations,” *Am. Inst. Chem. Eng. J.*, vol. 62, no. 6, pp. 1877–1897, 2016.
[24] M. Wu, J. G. Khinast, and S. Radl, “The Effect of Liquid Bridge Model Details on the Dynamics of Wet Fluidized Beds,” *Am. Inst. Chem. Eng. J.*, vol. 62, no. 6, pp. 1877–1897, 2016.
[25] S. Luding, “Introduction to discrete element methods: Basic of contact force models and how to perform the micro-macro transition to continuum theory,” *Eur. J. Environ. Civ. Eng.*, vol. 12, no. 7–8, pp. 785–826, 2008.
[26] S. Radl, C. Radeke, J. G. Khinast, and S. Sundaresan, “Parcel-Based Approach For The Simulation Of Gas-Particle Flows,” *8th Interantional Conf. CFD Oil Gas, Metall. Process Ind.*, no. June, pp. 1–10, 2011.
[27] D. M. Snider, “An Incompressible Three-Dimensional Multiphase Particle-in-Cell Model for Dense Particle Flows,” *J. Comput. Phys.*, vol. 170, no. 2, pp. 523–549, 2001.
[28] S. Radl and S. Sundaresan, “A drag model for filtered Euler-Lagrange simulations of clustered gas-particle suspensions,” *Chem. Eng. Sci.*, vol. 117, pp. 416–425, 2014.
[29] S. Radl, M. Girardi, and S. Sundaresan, “Effective drag law for parcel-based approaches - What can we learn from CFD-DEM?,” in *European Congress on Computational Methods in Applied Sciences and Engineering (ECCOMAS 2012)*, 2012, pp. 1225–1239.
[30] S. Radl and F. Municchi, “Spatial Filtering for Scale Bridging and Its Application to Transport in Dense Particle Beds,” in *Advances in Chemical Engineering*, vol. 53, Academic Press, 2018, pp. 1–312.
[31] C. Bierwisch, T. Kraft, H. Riedel, and M. Moseler, “Three-dimensional discrete element models for the granular statics and dynamics of powders in cavity filling,” *J. Mech. Phys. Solids*, vol. 57, no. 1, pp. 10–31, 2009.
[32] M. Sakai, H. Takahashi, C. C. Pain, J. P. Latham, and J. Xiang, “Study on a large-scale discrete element model for fine particles in a fluidized bed,” *Adv. Powder Technol.*, vol. 23, no. 5, pp. 673–681, 2012.
[33] E. L. Chana and K. Washinoa, “Coarse grain model for DEM simulation of dense and dynamic particle flow with liquid bridge forces,” *Chem. Eng. Res. Des.*, vol. 132, pp. 1060–1069, 2018.
[34] S. C. Thakur, J. Y. Ooi, and H. Ahmadian, “Scaling of Discrete Element Model Parameters,” *Powder Technol.*, vol. 293, pp. 130–137, 2016.
[35] C. Goniva, C. Kloss, N. G. Deen, J. A. M. Kuipers, and S. Pirker, “Influence of rolling friction on single spout fluidized bed simulation,” *Particuology*, vol. 10, no. 5, pp. 582–591, 2012.
[36] H. G. Weller, G. Tabor, H. Jasak, and C. Fureby, “A tensorial approach to computational continuum mechanics using object-oriented techniques,” *Comput. Phys.*, vol. 12, no. 6, p. 620, 1998.
[37] C. Kloss, C. Goniva, A. Hager, S. Amberger, and S. Pirker, “Models, algorithms and validation for opensource DEM and CFD-DEM,” *Prog. Comput. Fluid Dyn. An Int. J.*, vol. 12, no. 2/3, p. 140, 2012.
[38] J. Ai, J. F. Chen, J. M. Rotter, and J. Y. Ooi, “Assessment of rolling resistance models in discrete element simulations,” *Powder Technol.*, vol. 206, no. 3, pp. 269–282, 2011.
[39] R. Beetstra, M. A. van der Hoef, and J. A. M. Kuipers, “Drag Force of Intermediate Reynolds Number Flow Past Mono- and Bidisperse Arrays of Spheres,” *AIChE J*, vol. 53, no. 2, pp. 489–501, 2007.

[40] C. Hrenya, C. LaMarche, K. M. Kellogg, and P. Liu, “Cohesive Particle Flows: On the Relevance of Cohesive Energy Vs. Cohesive Force Descriptions,” in *American Institute of Chemical Engineers Annual Meeting*, 2016.
[41] P. Darabi, K. Pougatch, M. Salcudean, and D. Grecov, “A novel coalescence model for binary collision of identical wet particles,” *Chem. Eng. Sci.*, vol. 64, pp. 1868–1876, 2009.
[42] C. M. Boyce, A. Ozel, J. Kolehmainen, and S. Sundaresan, “Analysis of the effect of small amounts of liquid on gas–solid fluidization using CFD-DEM simulations,” *AIChE J.*, vol. 63, no. 12, pp. 5290–5302, 2017.

8. List of tables

9. List of figures

10. Nomenclature

Latin Symbols

a_i	Dimensionless filling rate	[-]
Bo	Bond number	[-]
c	Damping coefficient	[kg/s]
Ca	Capillary number	[-]
cg	Coarse-graining ratio	[-]
d	Diameter	[m]
D^*	Dimensionless separation distance	[-]
e	Coefficient of restitution	[-]
E_{kin}	Kinetic energy	[J]
f	Function	[-]
F	Force	[N]
g	Gravity	[m/s^2]
k	Stiffness	[N/m]
h_ε	Particle roughness	[m]
h_{ij}	Surface distance	[m]
h_0	Initial liquid height	[m]
h_{rup}	Rupture distance	[m]
I	Moment of Inertia	[kg m^2]
L_c	Contact loss energy	[J]
L_t	Dissipated energy	[J]
L_p	Liquid on Particle	[m^3]
m	Mass	[kg]
M	Moment	[N m]
n	Normal unit vector	[-]
p	Pressure	[Pa]
r	Vector to Particle	[-]
$\boldsymbol{r}_{ij}$	Distance between interacting particles	[m]
R	Radius	[m]
Re	Reynolds number	[-]

St_v	Particle Stokes number	[-]
t	Time	[s]
t	tangential unit vector	[-]
T	Torque	[N m]
u	Fluid velocity	[m/s]
v	Particle velocity	[m/s]
$\boldsymbol{v}_{n,0}$	Impact velocity	[m/s]
$\boldsymbol{v}_0$	Reference velocity	[m/s]
V	Volume	[m^3]
V_d	Domain Volume	[m^3]
$\boldsymbol{v}_t$	Particle terminal settling velocity	[m/s]
W	Work	[J]
Y	Young's Modulus	[Pa]

Greek

β	Interacting Particles radius ratio	[-]
$\beta_{p,i}$	Particle drag coefficient	[kg/(m^3 s)]
δ	Particle overlap	[m]
γ	Surface tension	[N/m]
ρ	Density	[kg/m^3]
θ	Contact angle	[rad]
μ	Dynamic viscosity	[Pa s]
Π	Dimensionless key figure	[-]
μ_r	Rolling friction coefficient	[-]
υ	Kinematic viscosity	[m^2/s]
ν_{poi}	Poisson ratio	[-]
ϕ	Volume fraction	[-]
ϕ_m	Mobility coefficient	[-]
$\boldsymbol{\omega}$	angular velocity	[1/s]

Sub/Superscripts

*	Dimensionless parameter
avg	Average
cap	Capillary
coh	cohesive
cont	contact
crit	Critical
d	Damping
drag	Drag
eff	Effective
f	fluid
g	gas
i, j	particle indices
k	spring
l	liquid
m	Mobilization
max	Maximum
n	Normal
p	Particle
prim	Primary particle
parcel	Coarsened particle
r	rolling
ref	reference
rel	relative
s	solid
t	tangential
vis	viscous

11. Appendices

11.1. Appendix A.1: EPSD Model

In the following equations, all parameters that are used in the EPSD and EPSD2 models are described:

$$\Delta M_{r,t+\Delta t}^{k} = \Delta M_{r,t}^{k} + \Delta M_{r}^{k} \tag{84}$$

$$\left|\Delta M_{r,t+\Delta t}^{k}\right| \leq \boldsymbol{M}_{r}^{m} \tag{85}$$

$$\boldsymbol{M}_{r}^{m} = \mu_r \, R_{eff} \, \boldsymbol{F}_n \tag{86}$$

$$c_r = \eta_r \, c_r^{crit} \tag{87}$$

$$c_r^{crit} = 2\sqrt{I_r \, k_r} \tag{88}$$

$$I_r = \left(\frac{2}{I + m_{prim} \, r_{prim}^2}\right)^{-1} \tag{89}$$

11.2. Appendix A.2: Stiffness Scaling

The cohesive force acts like:

$$m_{eff} \, \ddot{\delta}_n = k_n \, \delta_n - c_n \, \dot{\delta}_n - F_{coh} \tag{90}$$

At max. overlap $\delta_{n,max}$, $\dot{\delta}_n$, and $\ddot{\delta}_n$ are zero. For that reason, the particle stiffness can be expressed as:

$$k_n = \frac{F_{coh}}{\delta_{n,max}} \tag{91}$$

The effective Young's modulus Y_{eff} can be determined with the definition of the normal spring stiffness from the Hooke contact model in LIGGGHTS:

$$k_n = \frac{16}{15}\sqrt{R_{eff}} \, Y_{eff} \left(\frac{15 \, m_{eff} \, v_{n,0}^2}{16\sqrt{R_{eff}} \, Y_{eff}}\right)^{1/5} \tag{92}$$

The Young's modulus Y is calculated with:

$$\frac{1}{Y_{eff}} = \frac{(1 - \nu_{poi,1}^2)}{Y_1} + \frac{(1 - \nu_{poi,2}^2)}{Y_2} \tag{93}$$

where ν_{poi} is the Poisson ratio. The viscoelastic damping constant for normal contact is then determined from:

$$c_n = \sqrt{\frac{4 \, m_{eff} \, k_n}{1 + \left(\frac{\pi}{\ln(e_n)}\right)^2}} \tag{94}$$

11.2.1. Collision tests

The collision tests were performed with particle diameter 0.05 [m] and a liquid loading of 0.001. As can be seen in Table 11-1, the actual overlap when setting the dimensionless filling rate to 0.005 is significantly higher than the prescribed maximum overlap. Figure 11-1 shows the overlap of the tests with $a_i = 0$ and Figure 11-2 displays the outcome of the tests with $a_i = 0.005$.

Table 11-1: Overview collision test

Interaction	Dim.Fill-rate [-]	maxOverlap [%]	Sim.Overlap [%]
Particle–particle	0	1	1
Particle–wall	0	1	0.72
Particle–particle	0.005	1	14
Particle–wall	0.005	1	0.72

a) Particle–particle, $a_i = 0$

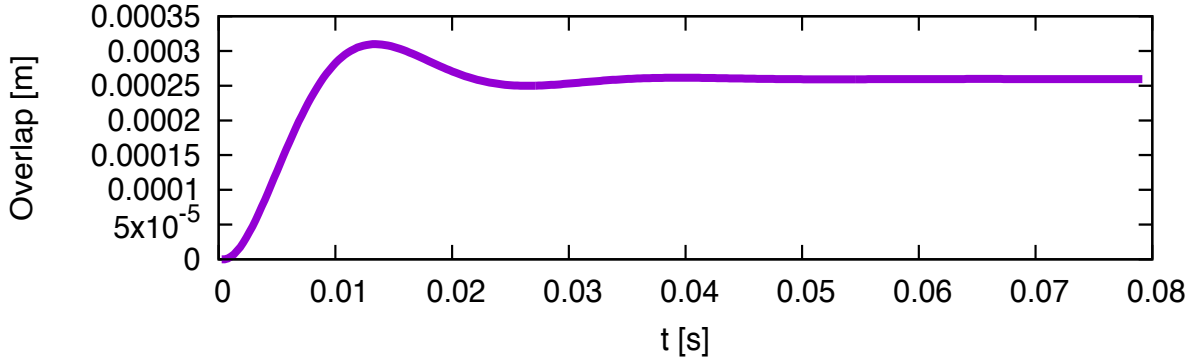

b) Particle–wall, $a_i = 0$

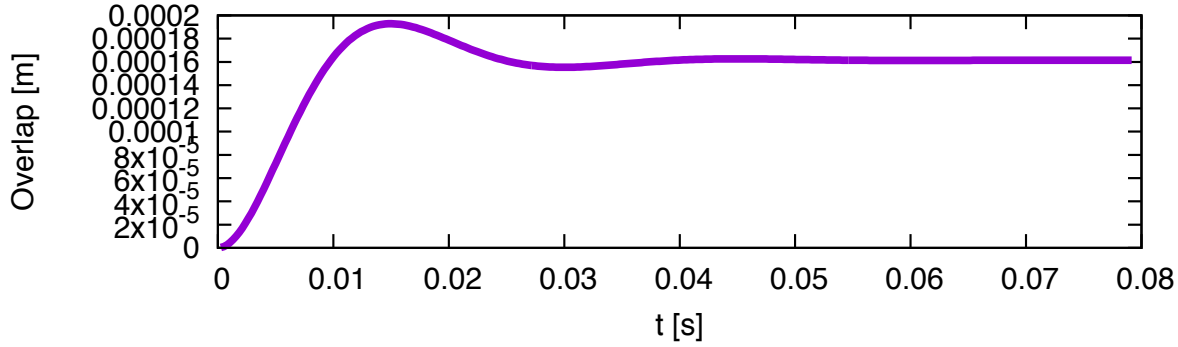

Figure 11-1: Overlap over time for $a_i = 0$

a) Particle–particle, a_i = 0.005

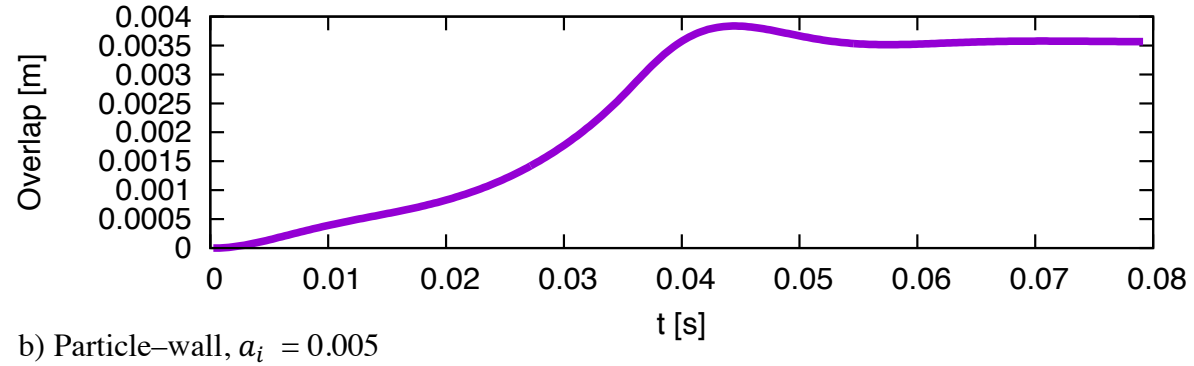

b) Particle–wall, a_i = 0.005

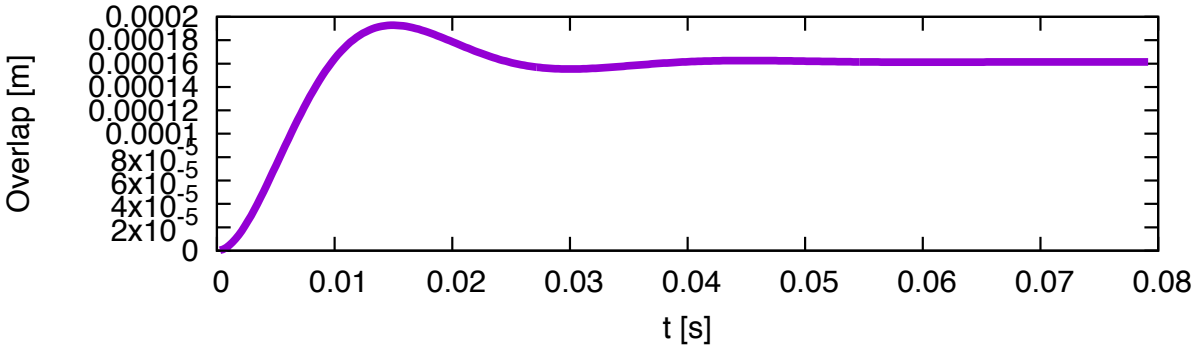

Figure 11-2: Overlap over time for a_i = 0.005

11.3. Appendix B: Box filling

The outcome of the big box-filling test for the Bond-scaled set-ups is displayed in Figure 11-3.

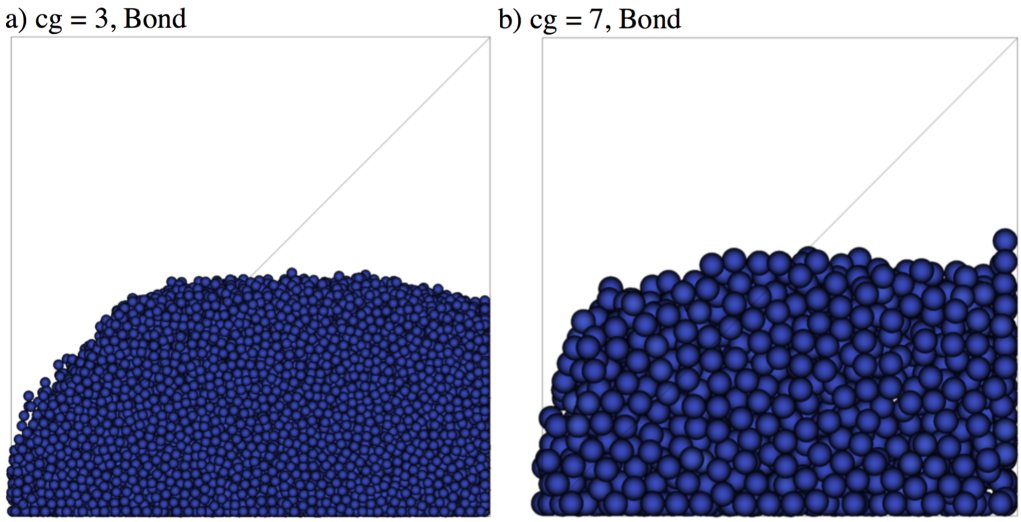

Figure 11-3: Filled simulation box with Bond scaling

11.4. Appendix C: Fluidization Test

11.4.1. Overall intersect

The intersect of the linear fit of the bed height data can be seen over different Bond numbers in Figure 11-4.

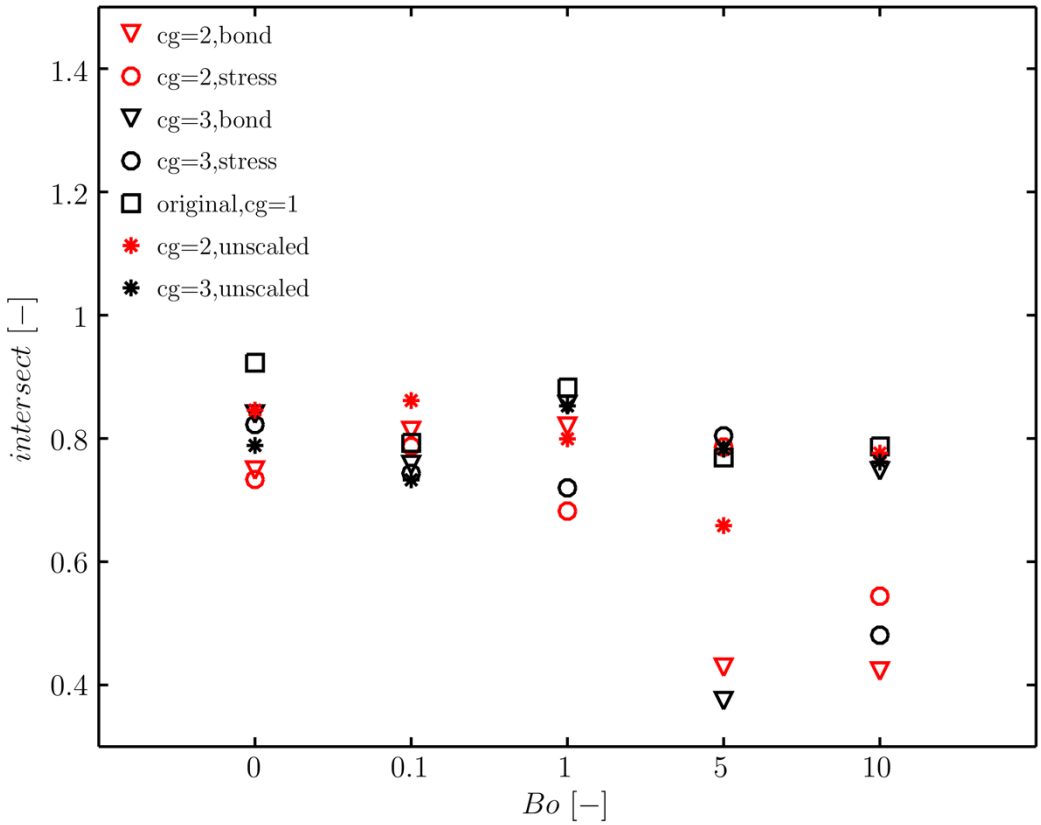

Figure 11-4: Overall results bed height fit, intersect

Table 11-2 shows the determined intersects of all tests.

Table 11-2: Results of the linear fit, intersect

		Bo=0	Bo=0.1	Bo=1	Bo=5	Bo=10
original,cg=1	*Intersect* [−]	0.923	0.793	0.883	0.769	0.787
cg=2,Bond	Dev.[%]	−18.91	2.49	7.14	44.27	46.35
cg=3,Bond	Dev.[%]	−9.06	−4.47	3.18	51.33	5.08
cg=2,stress	Dev.[%]	−20.52	−0.71	22.72	2.22	30.88
cg=3,stress	Dev.[%]	−10.87	−6.23	18.45	4.57	38.91
cg=2,unscaled	Dev.[%]	8.34	−8.66	9.45	14.37	1.39
cg=3,unscaled	Dev.[%]	14.55	7.56	3.39	−1.77	3.22

11.4.2. Average maximum overlap

The average maximum overlaps of the fluidization tests are summarized in Table 11-3.

Table 11-3: Overview of the average max. overlap

Avg. maximum overlap [%]					
	original,cg=1	cg=2,Bond	cg=3,Bond	cg=2,stress	cg=3,stress
Bo=0	12.44	8.01	5.07	13.27	10.67
Bo=0.1	17.63	7.33	4.95	12.49	10.56
Bo=1	12.12	5.37	3.34	8.43	7.77
Bo=5	6.36	2.53	1.56	4.06	3.65
Bo=10	3.29	1.51	0.79	2.85	2.47

11.4.3. Results slower acceleration of the gas velocity

As can be seen in Table 11-4 the variance of the slower accelerated gas ramps is higher than the variance of the basic case.

Table 11-4: Variance over different velocity ramps

Variance of the pressure drop data [Pa^2]			
	k_{ramp}	k_{ramp} 1/2	k_{ramp} 1/5
original,cg=1	3079.56	3361.60	3225.93
cg=2,Bond	1203.57	850.39	

Figure 11-5 and Figure 11-6 show the pressure drop and the bed height data of the tests with slower acceleration of the gas velocity.

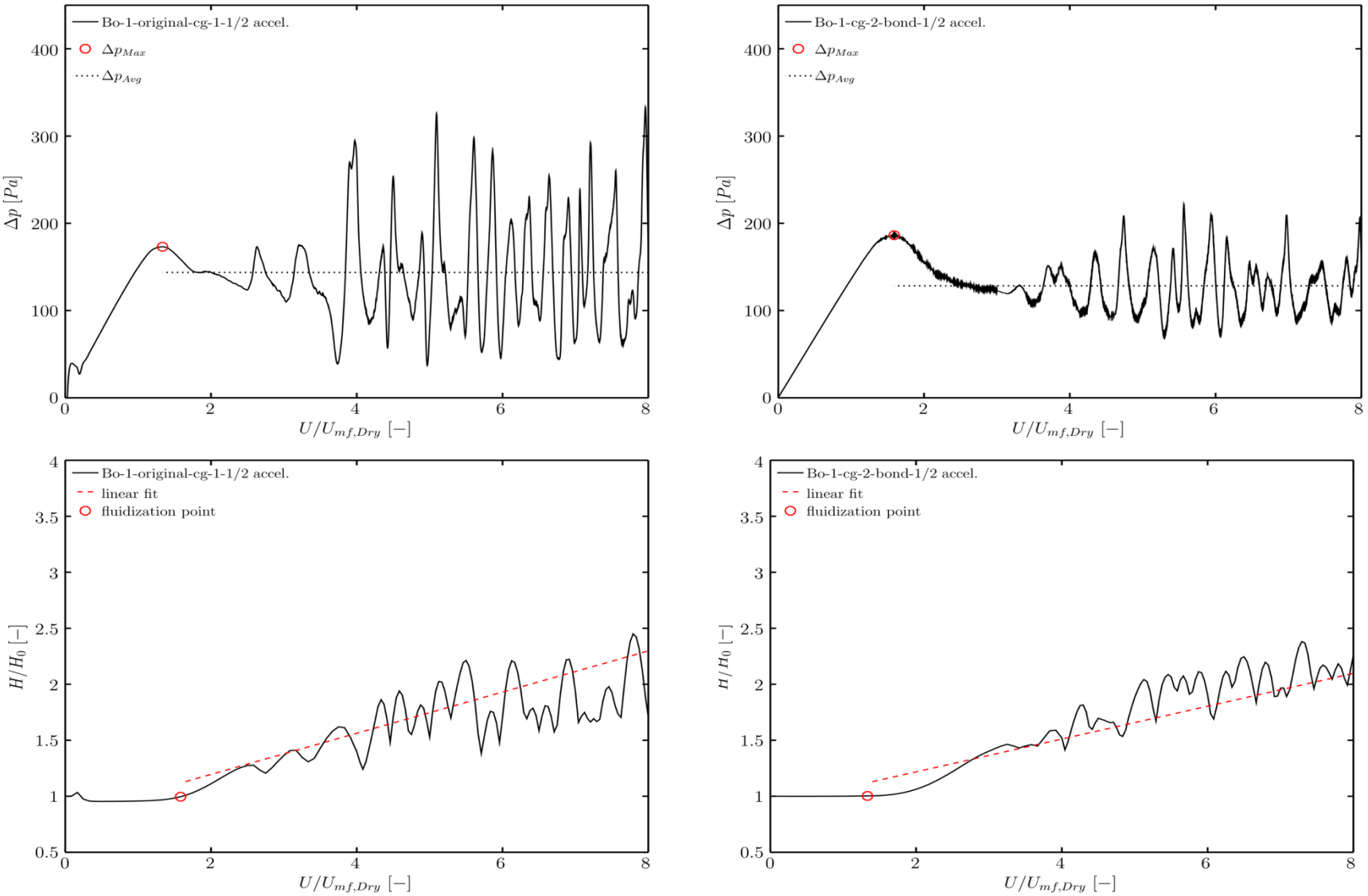

Figure 11-5: Pressure drop and bed height data for half acceleration at Bo = 1

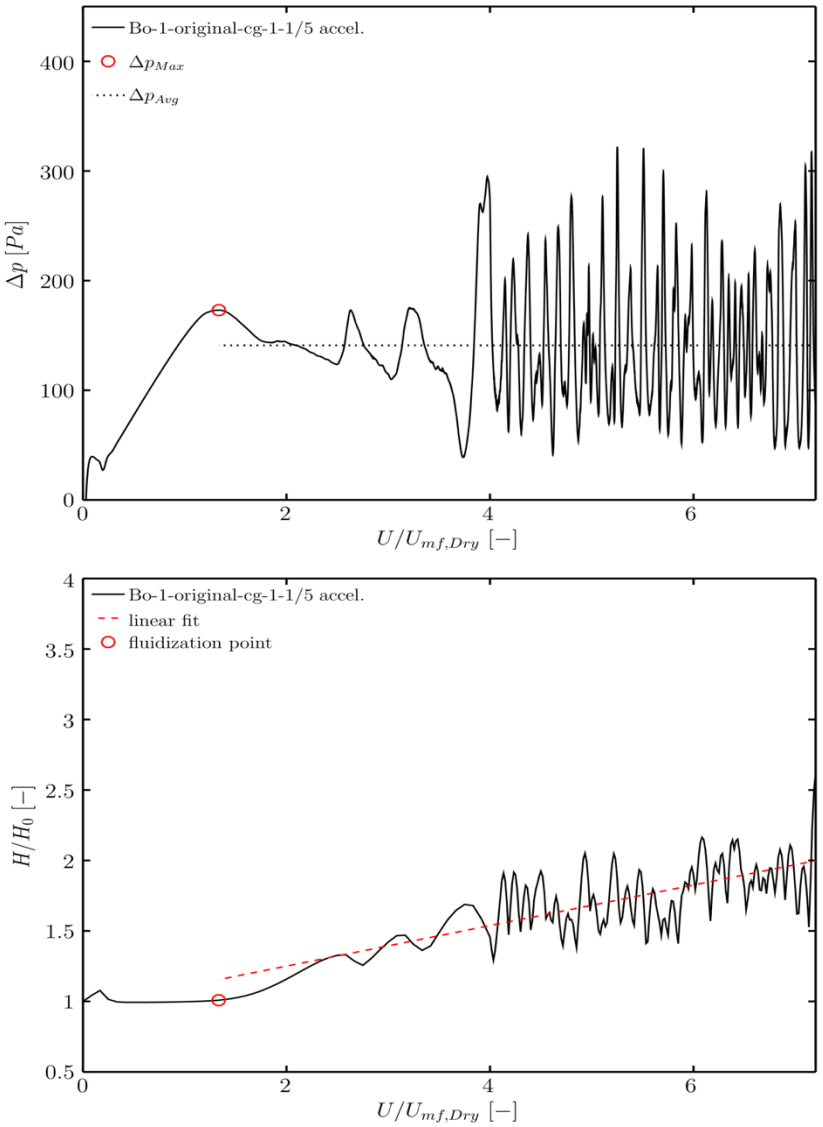

Figure 11-6: Pressure drop and bed height data for 1/5 acceleration at Bo = 1

11.5. Appendix D: Octave scripts

11.5.1. Minimum Fluidization Velocity and terminal settling velocity

The following code was used to estimate the minimum fluidization velocity and for the calculation of the terminal settling velocity. In the case of the terminal settling velocity, the particle volume fraction phiP was set to zero.

```
function y = beetstra2 (x)
    y=zeros(1,1);
    etaFluid=1.8e-5;
    dprimary=150e-6;
    phiP=0.64;
    Vp=dprimary^3*3.1415/6;
    rhoFluid=1.25;
    rhoP=2000;
    nuFluid=etaFluid/rhoFluid;
    rhoM=rhoP*phiP+rhoFluid*(1-phiP);
    uF=0;

    A=18*etaFluid/dprimary^2*(1-phiP);
    B=10*phiP/((1-phiP)^2)+(1-phiP)^2*(1+1.5*phiP^0.5);
    C=0.413/(24*(1-phiP)^2);
    D=(1-phiP)^-1+3*phiP*(1-phiP);

    ReP=abs((1-phiP)*dprimary*(uF-x(1))/nuFluid);
    betaP=A*(B+C*ReP*((D+8.4*ReP^-0.343)/(1+10^(3*phiP)*ReP^(-(1+4*phiP)/2))));

    y(1)=betaP/rhoP*(uF-x(1))+9.81*(1-rhoM/rhoP);
endfunction

figure;
t=linspace(0,0.90,1000);
y=lsode("beetstra2",-10^-6,t);
plot(t,y);
disp(y(end));
Umf=y(end);
```

11.5.2. Evaluation of the fluidization tests

```
close all;
clear;
clc;
%%laden von plotstyle
addpath("../../../")
%%%run("plotstyle.m");
c=pwd();
cas=strsplit(c,"/");
casename=cas{8}

%====================================%
% simulation data 1
%====================================%
rhoG=1.25;
UmfDry=0.027415;        %dry min. fluidization velocity [m/s]
veloc=inline("0.18276667*x");

%%%%%%%%%%load data
path = '../postProcessing/probes/0/p'; % 2.2.x
data = load(path);
[x,y]=size(data)
dp_sim = (data(:,2)-data(:,y))*rhoG; %conversion to Pa!
t_sim = data(:,1);
dp1=dp_sim';

dpMax=max(dp_sim(1:7500))

ind=find(dp_sim==dpMax);
UmfWet=veloc(t_sim(ind))./UmfDry
dpAvgRest=mean(dp_sim(ind+1:end))

varRest=var(dp_sim(ind+1:end))


velocities=veloc(t_sim)./UmfDry;
dp_data=[velocities' ; dp_sim']; %%save plot-data

%==================plot-dp-data==================%
fileN=sprintf('%s_dp.png',casename);
f3=figure();
set(f3,"visible","off","papersize",[12.0 12.0]);
plot(velocities,dp_sim,"k",UmfWet,dpMax,'x',"LineWidth",lineW);
title("Simulated Pressure
Drop","fontsize",fontsizeHeader,"fontweight",fontW,"FontName",fontstyle);
h=legend("dP ");
set(h,"fontsize",fontsizeLeg,"FontName",fontstyle);
xlabel("U/Umf,dry","fontsize",fontsizeLab,"FontName",fontstyle);
ylabel("dP [Pa]","fontsize",fontsizeLab,"FontName",fontstyle);
ylim([0 400]);
xlim([0 10]);
print(f3,fileN);

%===============bed height===========%
pwd();
cd ../../DEM/post;
delimiterIn=' ';
headerlinesIn=9;
impData=importdata('dump.staticBed',delimiterIn,headerlinesIn);
rawdata=struct2cell(impData);
data=cell2mat(rawdata(1));
```

```
%evaluation
zpos=data(:,2);
staticHeight=quantile(zpos,0.99)        %definition bei Boyce et al
numfiles=120;
r=20000;
myDynData=cell(1,numfiles);
dynHeight=zeros(2,numfiles);
cfd=2500;
for k=1:numfiles
    dynHeight(1,1)=1;
    dynHeight(2,1)=0.000;
    filename=sprintf('dump%d.dynBedHeight',r);

    myDynData=importdata(filename,delimiterIn,headerlinesIn);
    rawDynData=struct2cell(myDynData);
    dynData=cell2mat(rawDynData(1));
    zpos2=dynData(:,2);
    dynHeight(1,k+1)=quantile(zpos2,0.99)/staticHeight;
    dynHeight(2,k+1)=cfd*5e-6;
    cfd=cfd+2500;
    r=r+2500;
end

velocity=veloc(dynHeight(2,:))./UmfDry;
minfl=(velocity-UmfWet)./UmfWet;
[v,i]=min(abs(minfl));

height_data=[velocity;dynHeight(1,:)]; %save plot-data

%%%linear fit
linfit=polyfit(velocity(i:end),dynHeight(1,i:end),1)
testplotx=velocity(i:end);
testploty=linfit(1)*velocity(i:end)+linfit(2);

cd ../../CFD/octave ;

file2=sprintf('%s_bedH_data.txt',casename);
fid=fopen(file2,'w');
fprintf(fid,'%f %f\n',height_data);
fclose(fid);

file3=sprintf('%s_dp_data.txt',casename);
fid2=fopen(file3,'w');
fprintf(fid2,'dpMax[Pa]= %f\n',dpMax);
fprintf(fid2,'dpAvgRest[Pa]= %f\n',dpAvgRest);
fprintf(fid2,'varRest= %f\n',varRest);
fprintf(fid2,'UmfWet= %f\n',UmfWet);
fprintf(fid2,'slope= %f\n',linfit(1));
fprintf(fid2,'intersect= %f\n',linfit(2));
fprintf(fid2,'dp time data\n');
fprintf(fid2,'%f %f\n',dp_data);
fclose(fid2);
```

11.5.3. Evaluation of the periodic box data

```
close all; clear; clc;
run("plotstyle_v2.m");
currDir = pwd;
%%- paths for general installation
utDIR=getenv ("CFDEM_UT_DIR");
utilityPath = strcat(utDIR,"/multiphaseFlowBasics/")
addpath(utilityPath);
tutDIR=getenv ("CFDEM_TUT_DIR");
CFDPath = strcat(pwd,"/../")
uSlipFile1 = "averageProps/0/uSlip";
uSlipFile2= "averageProps/0.64/uSlip";

f=strsplit(CFDPath,"/");
bez=f(6);
l=strsplit(bez{1},"_");
leg=strcat(l(3),"-",l(4),"-original-cg-1");

cd([CFDPath])
%====================================%
% simulation data
%====================================%
data1= load(uSlipFile1);
data2= load(uSlipFile2);

uSlip_sim       =[data1(:,5)' data2(:,5)'];
phi_sim         =[data1(:,2)' data2(:,2)'];
t_sim           =[data1(:,1)' data2(:,1)'];
%====================================%

%====================================%
% analytical calculation
%====================================%

%%%%ParticleProperties
dragLaw          = 1;
dragName         = 'Beetstra'
dprimary         = 150e-6 ;
g               = 9.81
rhoFluid        = 1.3
rhoP            = 2000;
nuFluid         = 1.3846e-5;
etaFluid        = nuFluid * rhoFluid
uTerm            = 0.8562;
[uSusp, ReSusp] = uSettlingSphereSuspension(  dprimary, rhoP, g, etaFluid, …
                        rhoFluid, mean(phi_sim), dragLaw ); % ©Stefan Radl

T = uTerm./g;                    %reference time
tDimLess = t_sim./T;
uSuspDimLess = uSusp ./ uTerm;
uSlipDimLess = uSlip_sim ./ uTerm;

vecplot=[tDimLess; uSlipDimLess];
[vectime b c]=unique(vecplot(1,:));
vecU=vecplot(2,b);

cd([currDir])
searchTime=5.0;
[val ind]=min(abs(tDimLess-searchTime));
UsUt=mean(uSlipDimLess(ind:end))
mean(vecU(ind:end))
varU=var(uSlipDimLess(ind:end));
```

```
%%Save to File
file2=sprintf('%s_data.txt',bez{1});
fid=fopen(file2,'w');
fprintf(fid,'uslip/ut= %f\n',UsUt);
fprintf(fid,'variance= %f\n',varU);
fclose(fid);

%%%%%%BEGIN USER INPUT
graphics_toolkit("fltk");
fontSize = 14;
resolution  = 450;
plotSkip=100;
fontsizeLeg=12;
%%%uslip/ut
figure();
hold on;
plot(vectime(1:plotSkip:end),vecU(1:plotSkip:end));
plot([0 max(tDimLess)], [uSuspDimLess(1:plotSkip:end) uSuspDimLess(1:plotSkip:e
h=legend({leg{1},'analytic homogeneous Susp.'});
set(h,"location","northwest","fontsize",fontsizeLeg,"FontName",fontstyle,"fontw
legend boxoff;
set(gca,"fontweight","bold","linewidth",1.3,'fontsize',fontSize);
xlabel('$t / t_{Ref} \ [-]$','fontsize',fontSize,'fontweight','bold');
ylabel('$u_{slip} / u_t \ [-]$','fontsize',fontSize,'fontweight','bold');
%%xlim([0 60]);
ylim([0 2]);
t=bez{1}
t( t == "." ) = "_";
fileName=t;
print('-depslatexstandalone', fileName);
system (['latex ', fileName, '.tex']);
system (['dvips ', fileName, '.dvi']);
system (['gs -dNOPAUSE -dBATCH -dSAFER -sDEVICE=png16m ', ...
                '-dTextAlphaBits=4 -dGraphicsAlphaBits=4 -r', ...
                num2str(resolution),'x', num2str(resolution), ...
        ' -dEPSCrop -sOutputFile=', ...
        fileName, '.png ', fileName, '.ps'])
delete('*.tex','*.dvi','*.log','*.aux','*.eps')
```